

**Rotation and Torsional Stress Sensing
via Coherent Optics**

by

Alan G. Beardsley

Submitted to the Department of Electrical Engineering and Computer Science

in Partial Fulfillment of the Requirements for the Degree of

Master of Engineering in Electrical Science and Engineering

at the Massachusetts Institute of Technology

January 1995

Copyright Alan G. Beardsley 1995. All rights reserved.

The author hereby grants to M.I.T. permission to reproduce
and to distribute copies of this thesis document in whole or in part,
and to grant others the right to do so.

Author _____
Department of Electrical Engineering and Computer Science
January 27, 1995

Certified
by _____
George W. Pratt
Thesis Supervisor

Accepted
by _____
Frederic R. Morgenthaler Leonard A. Gould
Chairman, Department Committee on Undergraduate and M. Eng. Theses

MASSACHUSETTS INSTITUTE
OF TECHNOLOGY

AUG 10 1995

LIBRARIES

Barker Eng

Rotation and Torsional Stress Sensing via Coherent Optics
by
Alan G. Beardsley

Submitted to the
Department of Electrical Engineering and Computer Science

January 27, 1995

In Partial Fulfillment of the Requirements for the Degree of
Master of Engineering in Electrical Science and Engineering

ABSTRACT

Within the field of optical metrology (light-based measurement), lidar (light-based radar) and laser doppler velocimetry have been used for several years to perform remote sensing of rotational and translational velocity. Many configurations and techniques have been developed for the measurement of moving objects of widely-ranging size, distance, speed, and surface characteristics, from interplanetary space probes and satellites, to air molecules in a gas jet. This thesis explores the development of a practical precision rotational velocity sensor based on the use of coherent (laser) light sources and various kinds of diffraction gratings. This sensing technique is applied to rotating objects, upon whose surfaces diffraction gratings have been attached. The technique can be repeated at multiple points along the object's axis of rotation, to illuminate the differential velocities due to twisting or torsional stress.

Keywords: laser doppler velocimetry (LDV), rotary encoding, coherence and measurement, diffraction gratings.

Thesis Supervisor: George W. Pratt
Title: Institute Professor, Course VI-- EECS

CONTENTS

1. Introduction	1
2. Background / Methods	5
The Photo-Interrupter and Codewheel	6
Coherence	9
The Optical Homodyne	12
The Laser as a Coherent Source	14
Spatial Selection	15
Diffraction Gratings	16
Effect of Grating Curvature	20
Optical Elements	22
Interferometric Velocity Measurements	22
Limits of the Photointerrupter (codewheel) Technique	23
The Coherent Laser Doppler Velocimeter	25
3. Results	27
Optical Experiment: Configurations	27
Optical Experiment: Construction	32
Optical Experiment: Results	34
Post-Processing	35
4. Discussion	40
Target Surface -- spatial preparation	42
Recombination	45
Summary Uncertainty Model	46
Detection	47
Processing -- Burst Analysis	47
Torsional Stress Sensing and Analysis	49
Product Development	50
Summary	51
References / Bibliography	54
Acknowledgements	57
APPENDICES	
A. Diffraction grating modelling in MathCAD(tm)	58

LIST OF FIGURES

1-1) Schematic diagram of the coherent differential Laser Doppler Velocimeter	3
1-2) Experimental arrangement for the coherent differential LDV	3
2-1) Ideal photo-interrupter and detection schemes.	6
2-2) Fourier transform of squarewave with noise	8
2-3) Laser Doppler Anemometry (LDA) setup	11
2-4) Doppler shift from moving surface	11
2-5) Optical Homodyne illustration	12
2-6) a) Diffraction orders	
b) Scatterer construction	17
2-7) a) Flat grating, curved screen	
b) Curved grating, curved screen	20
2-8) Effect of number of gratings illuminated	21
2-9) Effect of duty factor of grating (Fourier method)	21
2-10) Fine Structure of 0-order from grating codewheel	24
2-11) CD-technology based absolute encoder (example)	24
3-1) Single order LDV with reference beam configuration	27
3-2) LDV combining the zero and 1 order	28
3-3) Double diffraction setup	29
3-4) Symmetrical Double-diffraction setup	31
3-5) Experiment configuration	32
3-6. Experiment & processing block diagram	33
3-7) Linear motion of glass grating (reference sample, $p = 10 \text{ } \mu\text{m}$).	36
3-8) Linear motion adhesive-backed diffraction grating D1, $p = 2.0 \text{ } \mu\text{m}$	36
3-9) Sample traces of a.) LDV detector output	
b.) codewheel squarewave (500 cycles/rev)	
c.) Fourier transform of (a.) with reference from (b.)	37
3-10) Rotary motion, $R = 0.5''$ disk	37
3-11) Rotary motion, $R = 2.0''$ disk	38
3-12) Doppler shift for high-speed rotation, $R = 2.0''$ disk	39
3-13) Rotary motion, $R = 1.0''$ disk	39
4-1) Coherent differential laser doppler velocimetry diagram (coplanar)	40
4-2 a) Features of the rotation	
b) Ideal and non-ideal gratings	43
4-3) Sources of uncertainty in the coherent differential LDV measurement	46
4-4) Codewheel (reference) velocity estimator uncertainties	46

LIST OF TABLES

3-1) Precision disk specifications.	32
---	----

1. INTRODUCTION

Every day, drills, saws, turbogenerators, drive shafts, and hundreds of other kinds of rotating systems undergo millions of revolutions. Designers of these spinning mechanical systems want to know how far they can push the limits of their materials. They can only get the proper insight into their models by having a sensing system with sufficient bandwidth and sensitivity.

Many configurations and techniques have been developed for the laser-assisted measurement of moving objects of widely-ranging size, distance, speed, and surface characteristics, from interplanetary space probes and satellites [28] to air molecules in a gas jet [13]. The premise of this M. Eng. thesis is that it would be highly desirable to have an instrument that can measure the speed of rotation of an object in real-time to unprecedented accuracy. The primary variable of interest is the angular velocity ω , which is the derivative of the phase angle ($\omega = d\phi/dt$) of the object about its axis. With an instrument of this type it should be possible to investigate the torsional (twisting) modes of spinning objects such as drive shafts.

We first considered the ultimate resolution possible with the light chopper or *photo-interrupter* circuit. This circuit, in many guises, is the basis of a large and active industrial metrology industry [21] [33]. Pursuing the light chopper idea to its extremes in precision and range leads into regions where

- features or profiles have dimensions comparable to or smaller than a wavelength, leading to diffraction effects, and
- single pure frequency, *coherent* light sources are needed-- that is, ones where the photons are aligned in frequency, polarization, propagation direction and phase.

The remote sensing and measurement of the velocity of moving objects has undergone a revitalization since the 1960's when *coherent* optical sources (i.e., lasers) first became available. A *coherent* source is one in which the constituent photons in the beam are sufficiently stable in their temporal and spatial propagation patterns that if they are split and recombined (at a slight angle), interference fringes can occur. In optical metrology (light-based measurement) these high-power, narrow linewidth, collimated beams yield powerful but subtle new techniques of measurement based on spatial and temporal correlation (fringe-forming) properties:

1959	First Laser developed
1964	<u>Laser doppler velocimetry (LDV)</u> proposed [11]
1970's	First implementations of LDV and LDA (laser doppler anemometry) development of lidar (light-based radar)
late 70's- 80's	Application of photon counting and photon correlation methods, real-time holographic interferometry, laser ring gyroscopes
late 80's- 90's	LDV Integration (semiconductor laser diodes, fiberoptics), development of laser time-of-flight velocimetry (LTV)

Laser doppler velocimetry (LDV) measurements are today used to sense motions as diverse as steel rolling and fluid and gas flow [5][16]. It has been suggested that "in some cases, industrial applications appear to require much higher accuracy than scientific applications: a very small deviation from nominal values may have significant economic consequences; it may also have a serious impact on the production quality" [30].

Advantages of coherent methods over other methods, such as incoherent light (scattering) and rf and microwave (radar) measurements, include higher spatial and temporal resolution, due to the smaller wavelength and wavelength spread of the electromagnetic energy used in the probing beam. The visible wavelength band approaches ($\sim 4\text{--}8\ \mu\text{m}$) have the additional feature of being easier to track and diagnose in an application environment, since the beams are often clearly visible.

In this thesis, the laser doppler velocimetry (LDV) technique, intermediate to *lidar* (light based radar) and *real-time holographic interferometry*, is explored and a working model constructed (see Figures 1-1 and 1-2.) In these LDV configurations, a coherent source beam is split by a diffraction grating attached to the spinning object under study, and two of the diffraction 'orders' are recombined to extract the doppler beat frequency proportional to the velocity.

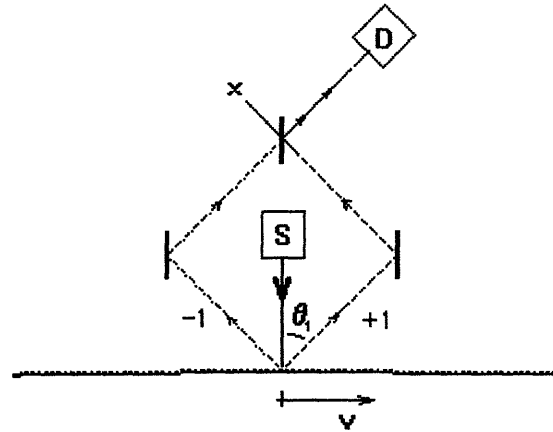


Figure 1-1. Schematic diagram of the coherent differential Laser Doppler Velocimeter

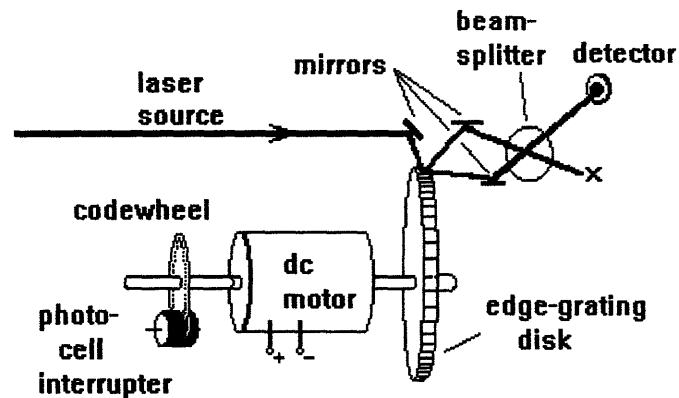


Figure 1-2. Experimental arrangement for the coherent differential LDV

The real-time capability inherent in the LDV velocity-sensing process enables the observation of structural dynamics such as *torsional stress modes* (twisting and untwisting under varying applied load), if the process is duplicated at two or more points along the object's axis of rotation.

In this work we pursue the development of a coherent homodyne differential laser doppler velocimeter to sense the rotational speed of a spinning object. This technique emerged from a consideration of the fundamental limitations of the *photo-interrupter* circuit, currently in wide use in industrial metrology. By extrapolation, the photointerrupter becomes a diffraction grating, and then interferometric methods (i.e., the homodyne receiver) are utilized to extract phase rate.

In summary, this thesis will describe a set of experiments performed with the coherent homodyne differential LDV technique, with the following goals:

- 1/ to learn about the special requirements associated with coherent optical experiments and their construction, and the issues surrounding general optical metrology
- 2/ to explore the configuration options and practical concerns surrounding this technique
 - a) forward and backscatter approaches (transmission vs. reflection modes)
 - b) mechanisms for spatial selection, including diffraction gratings
 - c) optical components including sources, waveguides, beamsplitters, and detectors
- 3/ to determine the resolution and accuracy achievable with the LDV technique, given various post-processing or analysis techniques
- 4/ to identify sources of error or uncertainty, and possible avenues of further improvement
- 5/ to consider the application of this technique to the sensing of torsional stress, and the additional sources of error in this process.

To these ends, Section 2 reviews the theory of coherence as applied to the laser doppler velocimeter, together with a discussion of general configurations, spatial selection (including diffraction gratings), and coherent detection. Section 3 describes the various experimental setups constructed and results obtained. Section 4 seeks to interpret these results in a variety of post-processing frameworks, assess the uncertainties present, and suggest improvements and applications in the area of torsion sensing.

2. BACKGROUND / METHODS

Measurement techniques that take advantage of the coherence properties of laser light sources include *lidar* (light based radar) and *real-time holographic interferometry*. In lidar, light pulses with a certain repetition rate, pulsewidth, and frequency envelope (chirp) are emitted in a beam and the reflected signal from a 'target' is received and processed for time delay (range) and doppler shift (range rate.) In holographic interferometry, successive snapshots are made of stress patterns on a metal surface, for example, by illuminating with crossed laser beams, which create a grid or reticle of interference fringes that overlay the surface, and graphically depict the plastically deformed areas of stress concentration.

In this thesis an intermediate technique called *laser doppler velocimetry* (LDV) is explored and a working model constructed. In this technique, a coherent source beam is scattered from a spinning object under study, and two 'orders' of reflection are recombined to extract a doppler beat frequency, proportional to rotational velocity. The differential LDV configuration described here essentially makes a point measurement of the transverse velocity of a diffraction grating. It can be operated in reflection or transmission mode. This velocimeter can then be implemented at multiple points along the object's axis of rotation (or potentially scanned) to obtain the velocity profile along a surface parallel to the object's rotation axis. We can thus observe the deformations or differential velocities due to *torsional stress* or twisting in a real-time mode.

This section will consider the general rotation sensing problem, introduced and illustrated by one of the simplest optical rotation-speed sensors, the *photo-interrupter & codewheel*. This will in fact be used as the reference metric for the coherent optical experiments described in the next section. The codewheel rotational velocity sensor example leads to a consideration of *diffraction gratings*

and *spatial confinement*, which is put to good use in the combinations of beams using the idea of *coherence*. The foundation configurations for both fringe-based systems -- sometimes called *laser doppler anemometry (LDA)*, and the homodyne or optical beat frequency *laser doppler velocimetry (LDV)* systems are introduced.

THE PHOTO-INTERRUPTER & CODEWHEEL

In metrology (of any kind) , precision measurements can only be attained with 1) stable references and calibration standards; 2) repeatable configurations, and 3) extremely sensitive --high-gain, low-noise sensing. An ideal photo-interrupter configuration for metrological purposes, then, starts with a narrow, collimated, monochromatic beam of stable intensity, interrupts it with a spatially periodic material or transmission profile of minimal width (the 'codewheel'), and finally detects the time signature of the energy that passes through via a low noise detection system. In the quantum limit we may speak of a sparse stream of photons serving this purpose.

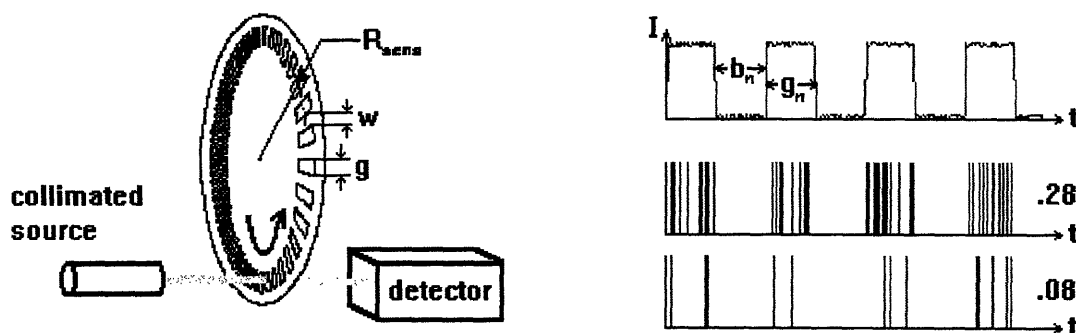


Figure 2-1. a) Ideal light chopper; b1) Analog detection;
b2,3) Photon counting (for two different values of photon number density)

Figure 2-1 illustrates the method and shows several traces representative of analog and photon counting detector outputs for an idealized experiment. The period of the (squarewave) output signal is the spatial period of the transmission profile ($b+g$) divided by the velocity of the

'codewheel' disk at the radius R_{sens} . The codewheel is so named because it often has irregular slot patterns or multiple tracks so that the phase angle ϕ of the rotation can be derived and not just the phase rate (rotational velocity [radians/sec] $\omega = d\phi/dt$.) If there are N total spoke and gap combinations or 'line pairs' (so called as they tend to be quite thin) an angular velocity ω (or rotational frequency $f = \omega/2\pi$)

$$T_n = \frac{distance}{velocity} = \frac{b_n + g_n}{\omega \cdot R_{SENS}} \quad \langle T \rangle \cong \frac{1}{f} \cdot N \quad (2-1a,b)$$

This is of course the expected result that for a disk with N slots rotating at f cycles per second, a frequency of $f \cdot N$ Hertz is observed at the detector, on average.

The actual period or frequency is modulated by the variations in the 'spoke' or gap width (b or g) [these variations affect the duty cycle $\sim g/(b+g)$ of the detected signal]. The pulsewidth of both the high and low parts of the cycle will be modulated by the velocity changes undergone by the spinning disk. Therefore if the source beam is narrow a high-resolution pulse-width determination can be made (given sufficient received power) that will be inversely proportional to the short-term rotational velocity or phase rate ω .

Instantaneous velocity variations are in effect integrated and 'sampled' at the transitions of the squarewave output (or photon burst arrival times), corresponding to the passing of an edge from the interrupter. These edge arrival times constitute a velocity sampling at a rate of $2N$ per rotation. If the widths b and g have sufficiently small deviation from their norm (or are stable and can be calibrated), this technique can yield good accuracy.

The edge arrival time is further modulated by uncertainties in the source spatial emission profile (i.e. beamwidth effects), background and thermal noise fluctuations, and diffraction or probabilistic effects from the interrupter profile. Below a certain intensity or number density (in the photon counting detector), the arrival time will be unreliable as a local ('instantaneous') speed indicator,

but a Fourier-decomposition will still yield the average speed -- photons would rarely be seen in the 'dead zone' between gaps.

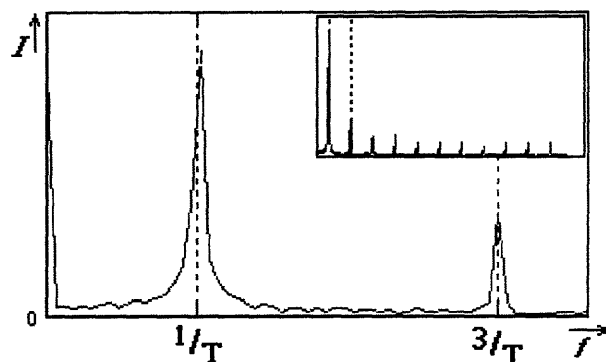


Figure 2-2. Fourier Transform of squarewave with noise

A Fourier transform of the squarewave output of the analog detector of Figure 2-1.b1 would appear as in Figure 2-2 above. A low-frequency or DC 'pedestal' appears due to large-scale fluctuations of the intensity envelope or non-symmetric overall duty cycle. The center frequency of the sinc function is at $f \cdot N = 1 / T$. The added broadening of the peak at $1/T$ is due to two factors: 1) intrinsic variations in the velocity of the rotation during the sampling interval, and 2) variations due to the measurement: individual duty factors for each line pair, short-term intensity fluctuations at the source, and beamwidth and numerical aperture effects. The figure also depicts the wideband thermal (shot) noise or *dark current* baseline, present in all available photodetectors.

There is in fact a large and active business today in industrial process control using some variant of the *photocell* idea to sense rotational rate. **Rotary encoders** are generally classed as *absolute encoding* (able to provide an output proportional to absolute phase [even after being turned off]), and *incremental encoding* (only able to provide phase-rate or relative phase information.) An absolute encoder, for example, might have several 'codewheels' or multiple tracks and a bank of emitters and detectors, such that any phase angle corresponds to a unique output code [33]. An incremental encoder might use an 'index pulse' or alignment pattern with a specific phase origin on

the codewheel, and a digital counter for keeping track of the line pairs as they go by [22].

Commercial products are available that can encode phase angle to better than 10^{-4} of a revolution (line pairs to 36,000!); phase rates (speeds) up to tens of thousands of RPMs [33]. The multitrack encoders can also utilize quadrature phase interpolation ('*multiplication*') to further improve resolution by an additional factor of ~ 4 [21].

As line pairs are made increasingly smaller, the line pair spacing becomes comparable to the wavelength of the light source (visible range $\sim .4\text{--}.8\ \mu\text{m}$.) Structures with periodic optical density (or reflectivity) variations of this length scale are known as *diffraction gratings*. Their reflection profiles are highly selective as to frequency and spatial direction. Like prisms, the reflection angles depend strongly on wavelength. Diffraction gratings also separate out secondary beams or *orders* of reflection. A great many uses have been devised for these gratings, in metrology, velocimetry, and elsewhere [7]. Before discussing applications we must introduce the idea of coherence.

COHERENCE

In searching for an improvement on the photo-interrupter technique, one is drawn to consideration of wave optics, diffraction and interference. The process of interference fringe formation requires that the beams of light have good phasefront stability; that is, that they be *coherent*. An infinite plane wave travelling in an isotropic, non-dispersive uniform medium would have perfect coherence. Correlations made between pieces of the wave selected at any time or place would identically match ones selected from a different time or place [18, 23, 44].

Coherence in this context is explained simply as the ability to form intensity fringe patterns or stable regions of constructive or destructive interference. If we consider two travelling planewaves, A and B, linearly polarized and incident on an observation plane, their field vectors will add by

superposition (2-2), and we will observe an intensity proportional to the squared modulus of the resulting field (2-3)

$$\vec{E} = E_A \cdot \vec{p}_A \cdot e^{j(\omega_A t - \vec{k}_A \cdot \vec{r})} + E_B \cdot \vec{p}_B \cdot e^{j(\omega_B t + \phi_{AB} - \vec{k}_B \cdot \vec{r})} \quad (2-2)$$

$$I = |\vec{E}|^2 \quad (2-3)$$

With natural light sources, typically, the electric fields at any given detector surface will have widely distributed states of polarization, directions of propagation (wave vectors), and phases. Even if the input light were collected and collimated to arrive parallel at the detector, and all polarization vectors were aligned to the same linear polarization axis, the phases of the incident photons would still be unevenly distributed, and tend to yield a uniform, chaotic illumination [32].

The intensity, I , will vary so as to produce distinct fringes across a region dS if most of the \vec{E} vectors line up in the same direction rather than simply adding randomly. That is, coherence is achieved (in Eq. 2-2 and more generally to include N incident waves) and visible interference fringes are formed when

- a) the (linear) polarization vectors \vec{p} are at least roughly parallel (or antiparallel),
- b) the colors or frequencies ω are the same and stable, such that their relative phase is stationary, $d\phi_{AB} / dt \cong 0$,
- c) one wave amplitude does not completely dominate the other $E_A \approx E_B$, and
- d) the wavevectors \vec{k} are nearly aligned, such that their common dot product with the position vector \vec{r} is relatively large along some axis.

In any real experiment each of these parameters is a random variable with an underlying, sometimes unknown, statistical distribution. Since in most velocity-sensing experiments these distributions will change in time, the analysis of coherence often involves making the correct generalizations about complex multiply-stochastic processes [8].

As a simple example, if two planewaves (or, more realistically, two Gaussian beams) of the same frequency ω and polarization orientation \mathbf{p} impinge upon an observation plane at a small angle θ ($\bar{\mathbf{k}} \cdot \bar{\mathbf{r}} = \frac{2\pi}{\lambda} \cdot \cos(\theta/2)$), then a set of parallel fringes result, at a spatial period s of $\sim 2\lambda / \sin(\theta)$.

This is equivalent to a hologram of a tilted plane, which is the interference pattern formed when a reference beam is superimposed on the (inclined) reflected image beam. This arrangement is the basis of the Twyman-Green interferometer, an instrument used to test optical flatness -- if the fringes are straight, the surface must be flat to fractions of a wavelength [20].

In *Laser Doppler Anemometry (LDA)*, the passage of a small scattering particle through a set of these interference fringes (Figure 2-3) produces a modulation proportional to velocity (V), with period $T = s/V$ [8, 41]. The center frequency of the laser source is also modified via a Doppler shift from the moving particle. See Figures 2-3 and 2-4.

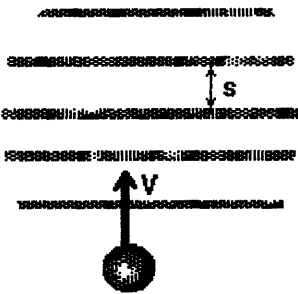


Figure 2-3. LDA setup

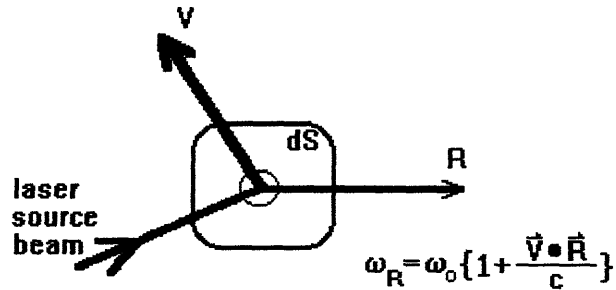


Figure 2-4. Doppler shift from moving scatterer

The *visibility* ν of the fringes or interference patterns is the contrast ratio of light to dark from wave crest to trough.

$$\nu = \frac{I_{\max} - I_{\min}}{I_{\max} + I_{\min}} \quad (2-4)$$

Visibility can also be thought of as a modulation depth of the available signal in the interfering mode [32]. The visibility can go to 1 for perfect coherence (in the low-background limit), where

the peaks of the dark fringes have zero intensity. Visibility serves as an important indicator of partial coherence, and is directly connected to signal-to-noise ratio in practical applications. It is useful as a summary of the energy lost to incoherence

THE OPTICAL HOMODYNE

If the wavevector and polarization directions of two beams of light are perfectly aligned ($\theta = 0$), then an observation plane at right angles to the propagation will be uniformly illuminated. Since perfect alignment and parallelism of two beams is no small feat, we can allow consideration of systems where a single fringe dominates the spatial region of interest (at the detector). If the two beams have different center frequencies, the overall intensity will vary at the difference (homodyne) frequency between the two input waves $|\omega_A - \omega_B|$, known as the *optical beat frequency* [44]. There will also be an oscillation at the sum frequency, $(\omega_A + \omega_B)$, which can be safely ignored as it is undetectable.

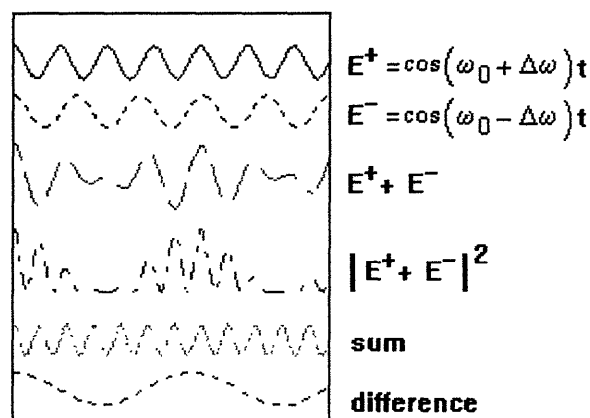


Figure 2-5. Optical Homodyne illustration

The optical beat frequency or *homodyne* technique is the one exploited in the present *laser doppler velocimetry* (LDV) work. Heterodyne systems, in which each beam is separately referenced to a third beam, are in fact used in some lidar-type applications [42].

Under some circumstances, partial coherence is attainable with incoherent light. Usually, a narrow frequency range and careful selection of the geometry for spatial filtering are required. For example, in Young's two-slit diffraction experiment, the slits or pinholes provide spatial

confinement to the extent that they behave as if two point sources were each emitting spherical waves [32].

The quality of coherence of the electric fields and of the resulting intensities may be characterized, respectively, by the *first-* and *second- order (temporal) coherence functions*. These functions represent the (auto- or) cross-correlation of the amplitude (or intensity) distributions within a temporal neighborhood $(t, t+\tau)$. Shown here are the *coherence factors*, which are the normalized form of the coherence functions.

$$G^{(1)}(\tau) = \frac{\langle E_i(t) \cdot E_i(t + \tau) \rangle}{\langle E_i(t) \cdot E_i(t) \rangle} \quad (2-5)$$

$$G^{(2)}(\tau) = \frac{\langle E_i(t) \cdot E_i(t + \tau) \cdot E_j(t) \cdot E_j(t + \tau) \rangle}{\langle E_i^2(t) \cdot E_j^2(t) \rangle} \quad (2-6)$$

Optical sources can be characterized by plotting the coherence factors vs. τ and obtaining a 'coherence profile'. The profile, in effect, establishes a timescale called the *coherence time* within which the sources remain stable enough to give rise to stationary interference patterns. The coherence time times the speed of light is the *coherence length*. Properly filtered sunlight might have a coherence length of a few millimeters, while standard HeNe lasers, for instance, have a coherence length of several tens of centimeters [19]. Any interferometric sensing experiments must work within this coherence length constraint. Fortunately, with balanced, differential systems, path lengths can be kept close by exploiting symmetry.

In a Michelson interferometer, for instance, a beam is split in half and one path is delayed relative to the other before they are recombined. If the delay exceeds the coherence time, or equivalently if the path length difference exceeds the coherence length, then the visibility of interference fringes will suffer. The fields become increasingly uncorrelated in the various degrees of freedom available (particularly phase). In lasers this is due mainly to spontaneous emission noise [35].

THE LASER AS A COHERENT SOURCE

The nearly-parallel, plane-polarized laser beam imparts a net flux of energy onto the 'probe volume' and from there to the detector, along a path determined by the overall Poynting vector \vec{S} constructed by the superposition of wave vectors \vec{k} .

$$\vec{S}(\vec{r}, t) = \int \vec{E}_i \times \vec{H}_i = \sum_i \frac{|\vec{E}_i|^2}{\eta_0} \cdot \vec{k}_i \quad (2-7)$$

With incoherent sources, the electric (or magnetic) field vectors of photons arriving at a given surface element tend to be of uncorrelated phase (ϕ_i) with each other, and so the fields tend to partially cancel within a certain spacetime neighborhood.

$$\vec{E}(\vec{r}, t) = \sum_i E_i \hat{p}_i \cdot e^{j(\omega_i t - \vec{k}_i \cdot \vec{r})} \cdot e^{j\phi_i} \quad (2-8)$$

The summation of a set of roughly equally-sized vectors with random phase (direction) distribution is called a 'random walk.' For a unit step length, the resulting expected rms (root mean square) distance from the origin after N steps is \sqrt{N} . In this case, the number of steps is the average photon number density during the detection interval, and the resulting distance from the origin is the rms electric field strength and the average electric field is zero.

By contrast, light from a laser or coherent light source has the vast majority of photons propagating in the same mode: nearly identical wavevector, phase, and polarization. The resulting field vector at a point in this type of beam is directly proportional to the number of steps N , or in this case the photon number density.

As mentioned above, the photodetection process generates a photocurrent proportional to the squared modulus of the total resultant electric field vector.

$$i(t; t + \Delta t) \propto \frac{\eta e}{hf} \cdot \left| \sum_{i=1}^N E_i \right|^2 \quad (2-9)$$

Therefore the intensity (and the photocurrent) for a coherent source goes as the square of the average incident photon number density [32].

$$\begin{array}{ll} \text{incoherent} & \text{coherent} \\ i(t; t + \Delta t) \propto N & i(t; t + \Delta t) \propto N^2 \end{array}$$

SPATIAL SELECTION

In interferometric metrology, applied to spinning objects, we seek to use coherent optics principles to the problem of extracting precise rotation rate sensing of a spinning disk or shaft. We begin by choosing a source known to have good coherence qualities; in this case a Hughes model 3225H-PC 10mW HeNe gas laser operating at 632.8 nm. The spatial confinement (concentration of energy in the laser cavity and the output beam) and the collimation, polarization alignment, and phase coherence of the laser make it a highly selective, sensitive tool for the investigation of various states and conditions of matter.

From general considerations of signal-to-noise ratio (SNR), maintaining coherence, and sensing a small target area, it is desirable to keep the sensing beam(s) tightly focused. This is an example of *spatial selection*, a guiding principle in coherence experiments. We desire to work with beams approximating planewaves, collimated, oscillating in the fundamental Gaussian transverse mode and with narrow linewidth and high modal stability.

With respect to receiving a strong return signal, several approaches have been put forth. One approach is to simply use whatever scattered light happens to come the way of the detector, or to use large collecting optics. A laser-illuminated irregular surface will yield a complex reflection pattern, including effects at several length scales. The *surface normal* vector and reflection coefficient fluctuate in a haphazard way over macroscopic distances, and will cause a modulation

of the received intensity. Also, the coherent illumination causes *speckle*, in which adjacent paths separated by a few wavelengths or less yield unwanted phasefront distortion and hot-spots.

Several ingenious velocity sensing methods have taken advantage of these features of irregular targets. Li et.al. [31] image the surface features, select a spatial Fourier component by projecting the 2D image through a 1D transmissive diffraction grating, and then autocorrelate in time to extract the phase rate or rotational velocity. Kitagawa and Hayashi [29] perform a similar operation based on speckle dynamics, in essence spatially Fourier-transforming the speckle pattern image through a fiber/detector array and then temporally autocorrelating.

DIFFRACTION GRATINGS

We chose another approach, in which we consider preparation of the target surface to channel the incident light into useful modes. In particular, a 1D *diffraction grating*, a spatially-periodic structure with lines of alternating high and low reflectance (or transmittance, as in the photointerrupter discussed above), can create a small set of spatially restricted diffraction *orders* or secondary beams.. The number of orders depends on the spatial period, which is usually on the order of a few times the illuminating wavelength itself. A brief review of diffraction grating theory as relevant to the experiment is now described [7,37].

The diffraction grating acts as a distributed spatial selection filter that, by imposing the right boundary conditions on the incident fields, selects and guides part of the incident light power into a small discrete set of orders, each with properties similar to the incident beam. These spatially-periodic grating structures can be fabricated in transmissive or reflective styles, and have become widely available through inexpensive holographic lithography technologies [14].

Light from any quality laser source, viewed microscopically within the beam, has very much the appearance of a monochromatic plane wave. We can exploit this property to sense motion by

bouncing a laser beam off of a moving diffraction grating. The diffraction grating is ideally an optically flat surface (whose variations in height are a small fraction of a wavelength) with a spatially periodic contour or reflectivity profile applied or etched into the surface material.



Figure 2-6a. Diffraction orders

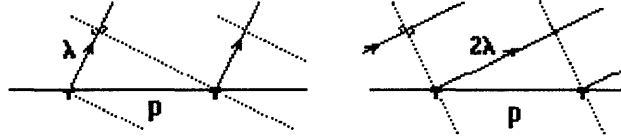


Figure 2-6b. Scatterer construction

The coherent laser light scatters into distinct 'orders' of diffraction where the wavefronts constructively interfere, and whose angles follow the classical diffraction grating relation

$$\sin(\theta_{\text{diffracted, order } m}) = \sin(\theta_{\text{incident}}) + \frac{m * \lambda}{p} \quad (2-10)$$

where m is the order number, λ is the wavelength, and p is the grating period or characteristic length, and all angles θ are measured from the normal to the grating surface. Diffracted order zero represents a mirrorlike ('specular') reflection of the beam. For each other order, the difference in path length between two adjacent scatterers (in the point scatterer model shown) is a whole number of wavelengths (Fig. 2-6b). Each order of diffraction is itself ideally a coherent beam with planewave behavior, as limited by the flatness and spatial uniformity of the grating. This planewave nature of each diffracted order holds true regardless of the incident polarization.

The intuitive, ray-optic picture with point scatterers as given above is correct for the ideal case, but of limited predictive power when deviations from ideality are present. In particular, we are concerned with a convexly curved, moving diffraction grating, with some amount of surface roughness and grating irregularity. To understand the actual behavior, given a finite laser source linewidth ($\Delta\lambda$), surface roughness and spacing irregularities (Δp), and beam divergences ($\Delta\theta$), we must go back to a rigorous diffraction theory.

Solutions to Maxwell's equations at the surface of a periodic (or nearly periodic) structure are generally represented by various approximation and perturbation techniques. Several analytical methods are available, including:

- 1.) classical Huygens-Fresnel wave theory or the Feynman QED sum-over-paths method, [7, 17]
- 2.) perturbation theory applied to boundary conditions of Maxwell's equations at the grating [10, 20], and
- 3.) Fourier optics and Fraunhofer approximations for the far-field [20].

Each analytical approach yields some insight useful for the successful modeling of the behavior of a curved, irregular, moving grating. They are all computationally intensive (see Appendix A.)

Highlights of the appendices MathCAD (TM) simulations are presented here.

Huygens-Fresnel theory (1) postulates that each point on an illuminated surface scatters light in the form of spherical waves, in-phase with the incident radiation. Non-flat surfaces simply obtain an additional phase delay at each scattering point due to the excess optical path needed to bring the planar phasefront to the surface. The computation for the observed intensity at an observation point P sums up equal contributions from all of the point sources with coordinates x,y along the surface S ; taking into account their individual phase delays due to distance from scatterer to observer [$D_p(x,y)$], plus any excess delay due to additional surface height $h(x,y)$.

$$I[P] = \left[\sum_x \sum_y e^{-j \cdot k \cdot D_p(x,y)} e^{-j \cdot k \cdot h(x,y)} \right]^2 \quad (2-11)$$

The Huygens-Fresnel sum is very time-consuming as it performs a sum of exponentials for each point on the scattering surface for every point on the observation screen. Spatial resolution in each domain (scattering surfaces and observation plane) must be a small fraction of a wavelength.

Other techniques seek to make generalizations of this approach -- the sum (2-11) is, however, a useful brute-force verification test for the other methods (see App. A).

If the grating surface is treated as a sinusoidal interface between air and a lossy dielectric substrate, then the reflected (propagated) mode wave vectors \mathbf{k}_m are related to the incident \mathbf{k} by $k_m = k \cdot \alpha_m \cdot \bar{x} \pm k \cdot \beta \cdot \bar{z}$, where $\alpha_m = \sin(\theta_m)$ and $\beta_m = \cos(\theta_m)$ when $\theta_m < \pi/2$ (TE case.) Following Dahleh et. al. [10], there are also grating modes, where β has a complex value, and (in general) transmission modes into the substrate as well. From the Helmholtz equation and electromagnetic boundary conditions (2), the total fields may be represented by summations of *Floquet* harmonics $\sum_m A_m \cdot \frac{e^{j \cdot \bar{k}_m \cdot \bar{r}}}{\sqrt{\beta_m}}$, with coefficients A_m depending on the incident field and its normal derivative, integrated along the diffracting surface.

In the Fourier optics technique (3), each diffraction grating element produces the Fourier transform of its 'pupil function' (illumination profile) in the far field. A grating with a squarewave profile, for example, appears as a set of rectangular slits illuminated by a planewave, which leads to a set of sinc functions for the far-field distribution at the observer screen. Since Fourier transforms represent a linear system, superposition of these diffraction patterns is valid. Therefore the transforms of each grating element illuminated, appropriately adjusted in phase and direction by the orientation of the grating element, add together to build up the total field at the observation screen [20]. The total field vector at each point at the screen, when squared, yields the observed intensity distribution. The figures shown here are generated with method (3) -- method (1) is used as a numerical test reference. All calculations assume ideal linear polarization.

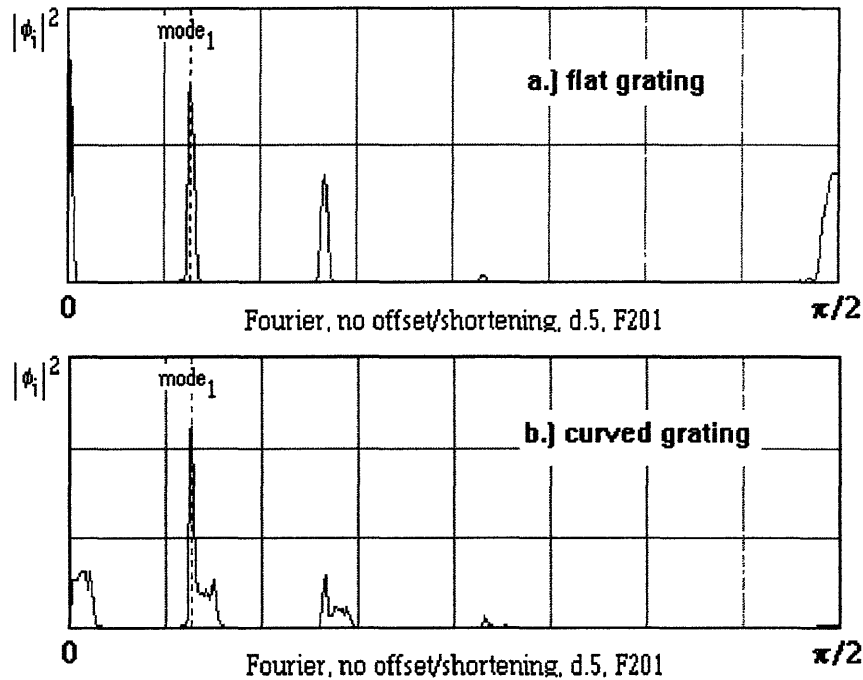


Figure 2-7) a) Flat grating, curved screen; b) Curved grating, curved screen

EFFECT OF GRATING CURVATURE

The application of the grating to a curved object yields a change in the diffraction pattern. As confirmed by the above analyses, the diffracted orders pick up an additional geometrical divergence equal to the curvature of the surface. In the Fourier analysis, for example, the grating element, constrained to the curved surface, becomes tilted relative to the observation plane, and fore-shortened in the observer direction. These are relatively small corrections to each grating element diffraction pattern.

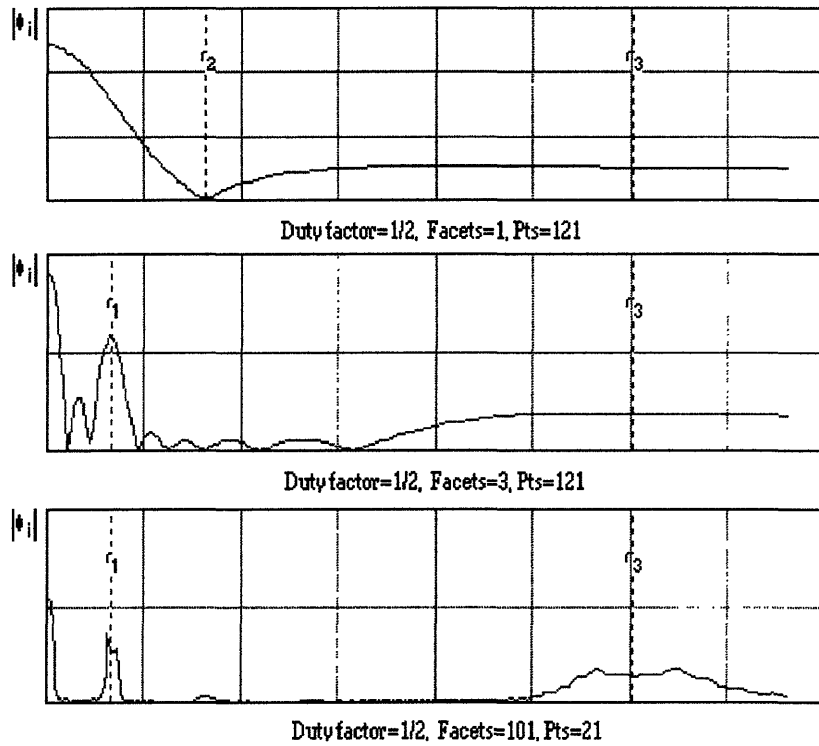


Figure 2-8) Effect of number of gratings illuminated

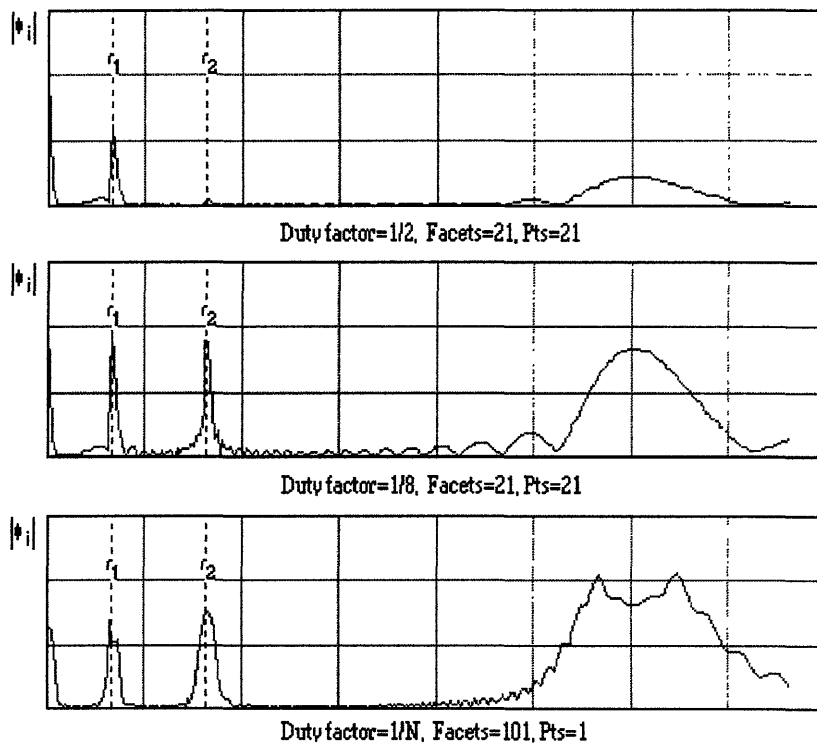


Figure 2-9) Effect of duty factor of grating (Fourier method)

The addition of curvature to the grating surface, as required for the convenient use of this technique with rotating targets, disrupts the delta-function nature of the diffracted orders (in a polar coordinate system.) The orders diffracted from a convex curved grating, with the radius of curvature in the grating cross-section plane, are centered at the same locations (azimuths), but now more diffuse than before. The divergence angle of each diffracted order is equal to m times the angle subtended by the laser spot incident on the target grating. For example, a 1mm. diameter spot at the grating ($w_1 = 1\text{mm}$) illuminates some 250 gratings ($p = 2$ microns). The divergence of the first order is $250 \cdot p/\rho$ or in this case, for a 1 cm. wheel, about 50 mrad.

Whereas concave gratings have been studied extensively, due to their usefulness in spectrometers, e.g. Rowland's circle, etc. [7], convex gratings have found a much narrower range of application.

OPTICAL ELEMENTS

Interferometers use fringe formation to investigate correlations between positions separated by as little as a fraction of a wavelength. Very often the means for splitting and combining light beams is a half-silvered mirror acting as a *beam-splitter*. Since interference effects only occur when light waves are acting as nearly-parallel planewaves, beam-splitters must be aligned very carefully, to present essentially one interference fringe at the detector. Diffraction gratings can also be used as beam-splitters, since they can also split and recombine coherent beams into coherent secondary beams, as discussed above. *Prisms* are also extremely fruitful devices for selecting in both the spatial and the frequency domains. Both prisms and gratings are highly frequency selective as to the diffracted angle and can be operated in transmissive and reflective configurations.

INTERFEROMETRIC VELOCITY MEASUREMENTS

Although the idea of coherent sources had been developed since the time of Fresnel, natural sources of such light were not forthcoming. However, with the development of the laser in 1959, a truly new light source came into being whose field vectors line up so perfectly in phase, frequency, and

direction, that the field oscillations can rip apart atoms of ordinary matter that get in the way. In a lower energy, non-destructive regime, the narrow linewidth and low noise of the laser output provides fertile ground for many types of remote sensing.

The idea of using interferometric fringing behavior to measure speed predates Rayleigh. When Michelson and Morley were searching for evidence of an 'ether drift' nearly 100 years ago, they utilized a carefully balanced, vibration isolated interferometer. They relied on the coherence properties of their light sources to the extent of getting a null result on a measurement requiring better than one part in 10^8 [34].

Grating approaches to interferometrics and metrology abound. One recently-published 'optical metrology' approach to rotation sensing shows a photodetector mounted behind a pair of transmissive *diffraction gratings* that rotate with respect to one another on the same axis, while the intensity is monitored within the Moire fringes [24].

LIMITS OF THE PHOTOINTERRUPTER (CODEWHEEL) TECHNIQUE

When the codewheel line pair spacing becomes so small that the light beam illuminates more than one opening, the intensity pattern at the photodetector becomes the 0-order diffraction pattern of the codewheel, acting as a transmissive diffraction grating. As shown by simulation with Fourier optics methods (see App. A), the 0-order transmitted beam has 'fine structure' to the spatial intensity profile. It can be shown that, if the grating (codewheel) is displaced by one-half a grating period (such that the grating elements now occupy the gaps in the previous orientation), then the intensity profile is also displaced. This follows from Babinet's principle that an intensity pattern formed by one spatial configuration of scatterers, when added to the pattern formed by the complementary configuration of scatterers, combines to form the overall intensity pattern expected from the source with no scatterers. A pinhole / detector combination then, situated so as to collect

only one small portion (e.g., one peak) of the intensity profile, will see an oscillation at the rate of line-pair passage.

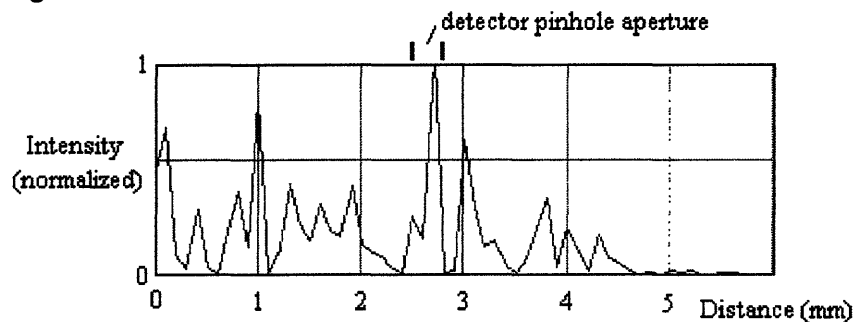


Figure 2-10. Fine Structure of 0-order from grating codewheel

In practice, the transmitted 0-order through the codewheel grating will contain irregularities and vibrations that will tend to make this approach impractical. The alternative is to keep the feature size large enough (or the probing beam small enough) to yield strong intensity contrast for each passing element. The 'pits' or reflectivity features in CD (*compact disc*) technology provide a feasible mechanism for rotary encoding. An encoder may be constructed from a specially-programmed CD codewheel, as shown in Figure 2-11. The use of multiple source/detector pairs (one per track) provides the absolute (phase) encoding. By duplicating the least-significant (fastest-varying) spatial tracks, and offsetting the tracks by 90° in phase, the resolution can be 'multiplied' as described above.

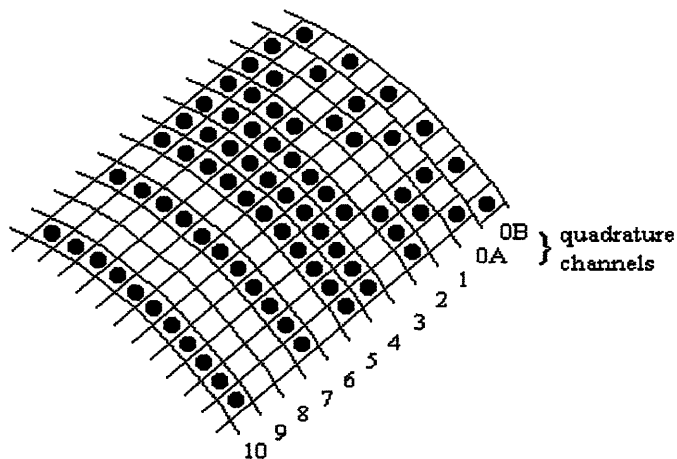


Figure 2-11. CD-technology based absolute encoder (example)

THE COHERENT LASER DOPPLER VELOCIMETER

The fringe-pattern based measurements used in laser doppler anemometry LDA have been introduced earlier in the discussion of coherence (see Fig. 2-3), as have techniques using speckle dynamics and spatial Fourier transforming. The remainder of the discussion will concern coherent homodyne measurements such as those used in laser doppler velocimetry LDV.

If a diffraction grating is given a non-zero lateral velocity, the +1 and -1 orders diffracted from the grating will possess Doppler frequency shifts proportional to the velocity. This can be seen as follows. The velocity component of the grating in the direction of the +1 order (the 'longitudinal component') is the scalar (dot) product of the velocity vector with the observation direction unit vector, or $v_{+1} = \vec{v} \cdot \vec{r}$. In the present case this becomes $v_{+1} = |\vec{v}| \cdot \sin(\theta_{R,1})$. Using the doppler

shift formula from Fig. 2-4 and the grating formula (2-10), the shift for the +1 order is

$$\Delta\omega = \omega_0 \frac{v \cdot \sin(\theta)}{c} = \omega_0 \frac{v \cdot \lambda}{c \cdot p} = 2\pi \cdot \frac{v}{p}, \text{ or } \Delta f = \frac{v}{p}. \text{ By symmetry, the -1 order is shifted}$$

down by this same amount $\frac{v}{p}$. Therefore the total frequency difference between the +1 and -1

orders, and hence the observed homodyne beat signal, is at a frequency (Hz) of $\frac{2 \cdot v}{p}$ for a lateral

velocity of v and a grating period of p . The 0-order diffracted beam will possess no net doppler shift, since (for normal incidence) there is no longitudinal component to the velocity. Higher-order diffracted beams (if any), i.e. for mode m , will be doppler shifted by a frequency of $\frac{m \cdot v}{p}$.

In the experiments described in the next section (see also Fig. 1-1), the coherent homodyne differential LDV method is utilized, with reflection-mode diffraction gratings, on a vibration-isolated optical bench. The idea is very simple. We aim the source beam at normal incidence to the grating, which is attached to the outer surface of a spinning disk. We collect the light from the +1 and -1 diffraction orders and direct these beams onto a beamsplitter. When the beams overlap at the beamsplitter and emerge coincident and parallel, a homodyne optical beat signal is observed

at the detector. This beat signal is proportional to the doppler shift, which is proportional to the velocity in the sensing direction. Symmetry keeps the path lengths equal and polarizations aligned.

Some configurations obtain the beat signal by recombining the 0-order with either the +1 or -1 order. This is known as the *reference beam* method, since the 0-order beam should have no doppler shift and will generally have a large intensity and superior planarity [9]. It should be noted that in some cases, the doppler-shift of the optical carrier can be detected directly, using a scanning Fabry-Perot interferometer as an optical frequency discriminator [6]. The coherent differential LDV approach seems to offer a better cost-effectiveness.

3. RESULTS

This section will describe the **Optical Experiment; configurations, construction, and results**, for the coherent laser doppler velocimetry (LDV) system. Also, the electronic **post-processing** of the detector output is reported.

OPTICAL EXPERIMENT: CONFIGURATIONS

The initial experiments use the +1 and -1 orders -- higher orders (if any) are discarded or blocked.

1. Single order, mixed with reference beam

In perhaps the simplest configuration (Fig. 3-1), the +1 (or -1) order of the grating is combined with a piece of the source (reference) beam, for example via a pair of beam-splitters.

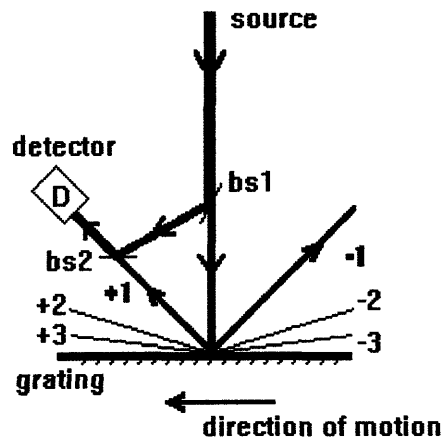


Figure 3-1. Single order LDV with reference beam configuration

Two beams arrive at the detector -- one from the source beam, as diverted by beamsplitter #1, and one from the target grating, via the +1 order. The two beams are recombined at beamsplitter #2.

The source-derived beam is centered at ω_0 (the laser source center frequency), while the beam from the target is at $\omega_0 + \Delta\omega$. Here $\Delta\omega$ is the (positive) doppler frequency shift due to the advancing grating. The resultant beam at the detector is then the superposition of the source and diffracted beams, and is at the new frequency of

$$\omega^+ = \omega_0 * \left(1 + \frac{v * \sin(\theta_{+1})}{c}\right) = \omega_0 + \Delta\omega,$$

so the detector beat signal for this configuration is centered at:

$$\omega_a = \omega^+ - \omega_0 = \omega_0 * \frac{v * \sin(\theta_{+1})}{c} = \Delta\omega$$

Similarly, the zero- order reflection from the grating (Fig 3-2) may be used instead of the source itself. In this case the 'reference' beam will include the amplitude and phase-modulating effects of surface roughness, target axial wobble, grating irregularity, and the like. Hence the resulting correlation process at the detector will tend to reject these low frequency and large-scale fluctuations. It should be noted here, though, that this single-ended configuration typically yields near-orthogonal polarizations at the detector plane, and hence gives weak visibility of interference signals without additional compensating efforts [9].

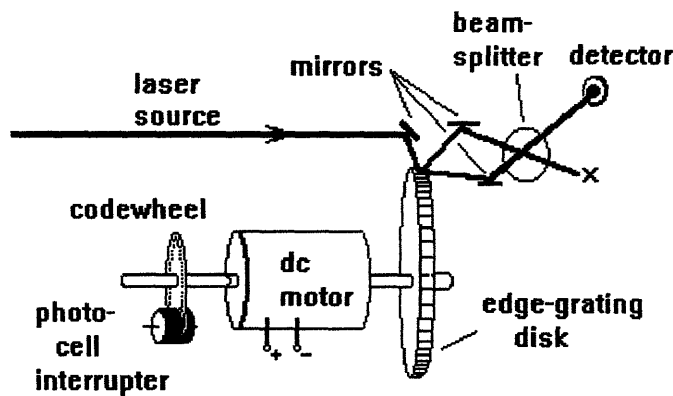


Figure 3-2. LDV combining the zero and 1 order

2. 'Crossbow' or double-bounce configuration

Another configuration (Fig. 3-3) uses a retroreflector to double-bounce the -1 order. In this case, the -1 order is reflected back to the grating -- it then propagates to the detector via a specular reflection from the grating (this is the zero order mirror-like mode from the new incident angle.)

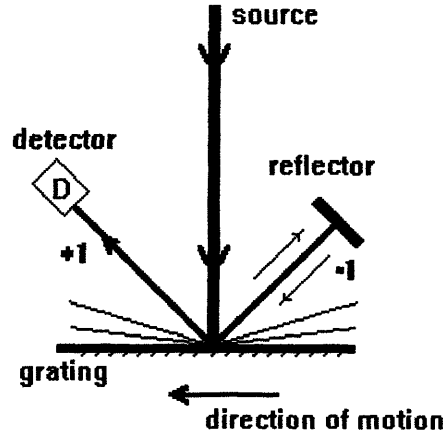


Figure 3-3. Double diffraction setup (see text)

In this double-diffraction setup, the -1 order beam is doppler shifted twice, once with frequency $-\Delta\omega$ relative to the source, and then after the reflection another $-\Delta\omega$ for a total shift of $-2\Delta\omega$. Therefore, two beams arrive (superposed) at the detector, one centered at frequency $\omega_0 + \Delta\omega$, the other at $\omega_0 - 2\Delta\omega$.

$$\omega^- = \omega_0 * \left(1 - 2 * \frac{v * \sin(\theta_{-1})}{c}\right) = \omega_0 - 2\Delta\omega$$

$$\omega_b = \omega^+ - \omega^- = 3 * \Delta\omega = 3\omega_0 * \frac{v * \sin(\theta_{+1})}{c}$$

In both configurations, two beams arrive superposed at the photodetector, nearly parallel and to some extent phase-coherent. The initial spectral intensity function $I(\omega)$ of the source has undergone a splitting (into the various orders), frequency (Doppler) shift, and recombination via superposition. The receiving photodiode behaves as a 'square-law' detector, providing an output photocurrent that is proportional to the incident intensity, or total electric field amplitude squared, averaged over the active area of the detector. Given certain stationarity and coherence constraints

on the laser source (as well as similar constraints on the temporal and spatial coherence of the

diffracted beams), discussed above, we can write

$$\begin{aligned} E_1 &= \cos[(k_0 + \Delta k)z - (\omega_0 + \Delta\omega)t] & E_1 &= \cos[(k_0 + \Delta k)z - (\omega_0 + \Delta\omega)t] \\ E_2 &= \cos[k_0 z - \omega_0 t] & E_2 &= \cos[(k_0 - 2\Delta k)z - (\omega_0 - 2\Delta\omega)t] \end{aligned}$$

$$\begin{aligned} E_1 + E_2 &= 2 \cos(kz - \omega t) \cos(\Delta kz + \Delta\omega t) \\ E_1 + E_2 &= 2 \cos(kz - \omega t) \cos(3\Delta kz - 3\Delta\omega t) \end{aligned}$$

$$\begin{aligned} \Delta\omega &= \omega_0 * \frac{v * \sin(\theta_m)}{c} = k_0 * v' \\ \Delta\nu &= \frac{\Delta\omega}{2\pi} \end{aligned}$$

Since the photodetector is unable to respond to frequencies above, let us say, a few hundred megahertz, it will only respond to the *beat signal* envelope (at frequency ω_a or ω_b) resulting from the superposition of the different input optical carrier frequencies [44].

While the double-diffraction setup was initially very promising, due to its simplicity, low parts count, ease of alignment, and elimination of the beamsplitter, it suffers from a fatal flaw that limits its usefulness in practical applications. When the target shaft, inevitably, wobbles or vibrates in the direction of the source beam (or has any component in this direction), the relative path lengths of the two arms are modulated by the vibration or wobble frequency. This in effect superposes a phase rate of change of the double-bounced beam, which averages in the long run to zero, but which is seen at the detector output as a very large broadening effect on the recovered frequency. This result has led us to consider only symmetric arrangements, in which any interfering beams at the detector have equal path lengths relative to the source.

3. Symmetric differential diffraction using ± 1 orders

The third configuration (Fig. 3-4) utilizes the same principle as the double-diffraction configuration just described, but instead of bouncing the -1 order back onto the target grating, instead routes this diffracted order to a beamsplitter where it is combined with the +1 order, similarly routed. Although the configuration now employs two mirrors, and requires careful alignment of both the mirrors and the beamsplitter, the overall geometry is symmetric and tractable. If symmetry is preserved throughout, the alignment proceeds much more readily. That is, if the source beam is at normal incidence with respect to the grating, and the mirrors and beamsplitter are adjusted to the same height (coplanar), then beam overlap and parallelism are greatly facilitated. Also, the path lengths will tend to be approximately equal and the polarizations of each plane-wave-approximated field component remain roughly aligned. These circumstances foster a high visibility of the interference beat signal, even with a laser source of relatively short coherence length.

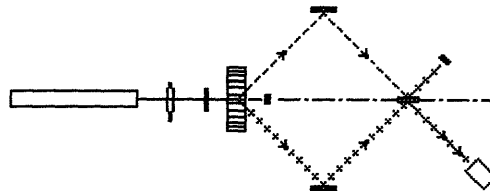


Figure 3-4. Symmetrical Double-diffraction setup (top view)

OPTICAL EXPERIMENT - CONSTRUCTION

A set of test disks were precision machined as follows:

DISK	RADIUS, in. (cm.)	MATERIAL	THICKNESS
			in. (cm)
1	0.500 +/- .0005 (1.770 +/- .0002)	PCS	1/4 (.635)
2	1.000 +/- .0001 (2.540 +/- .0001)	Lexan	1/4 (.635)
3	2.000 +/- .0001 (5.080 +/- .0001)	Lexan	1/4 (.635)
4 (HEX)	1.00 +/- .005 (diam., flat faces)	Stainless Steel	1/4 (.635)

Table 3-1. Test disk specifications

The disks were fastened to an Edmund Scientific 12V DC motor via a custom pressfit shaft mount assembly and thumbscrew. The motor was driven by a constant-current, constant-voltage power supply (**Harris Laboratories** model 855C). Two different types of adhesive-backed diffraction grating film were applied to the edge surfaces of the disks, such that the grating rulings were parallel to the axis of rotation (transverse to the disk edge.) A **Hughes** 10mW HeNe laser was directed at the edge of the disk. A series of optical elements (lenses, mirrors, beamsplitter, field stops, pinholes) were assembled and aligned into the differential configuration described above.

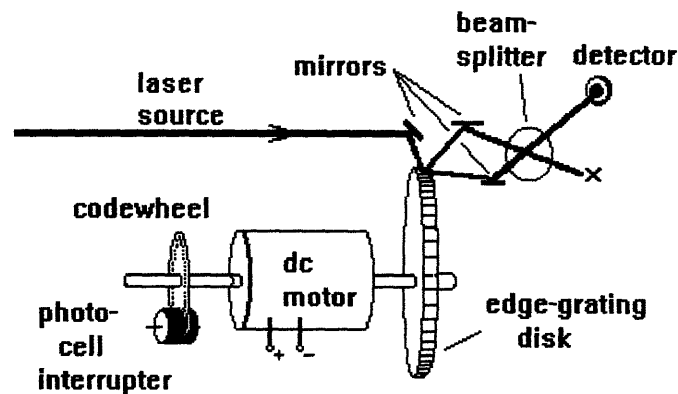


Figure 3-5. Experiment configuration

A PIN planar-diffused silicon photodiode detector (**United Detector Technology** model PIN-10DP) was mounted, together with a 35 micron wide pinhole aperture, on a low-vibration optical

bench mount. The output of the photodiode was coupled via a preamp (UDT model 1130a) to a high-pass filter (Krohn-Hite model 3100A), and to the input stage of an ANALOGIC (Data Precision) DATA 6000A multifunction waveform analyzer. In later experiments, a Hewlett-Packard HFBR-2456 integrated detector / preamp package was used for its greater detection bandwidth (to >125 MHz). The H-P detector had a very small active area (designed for multimode fiber use <100 um spot size), and hence did not need a pinhole aperture.

Phase rates, or rotational velocities, derived from the coherent optical technique were compared against reference (control) measurements from a standard commercial rotary encoding scheme. A Hewlett-Packard HEDS 9140 series rotary encoder circuits were used to obtain digital signals that encode the rotational rate of the codewheel. A codewheel of thin steel, stamped with 500 slots at the sensing radius of 11 mm., was affixed to the DC motor shaft and mounted into a sensor housing which uses an LED and lensing array, together with photodiode detectors, to generate a pair of quadrature digital outputs (90 degrees electrically out of phase) at 500 cycles per rotation as the codewheel slots periodically eclipse the photocell. Additionally, the sensor unit generates an 'index pulse' at *top dead center* as determined by alignment patterns built into the codewheel [22].

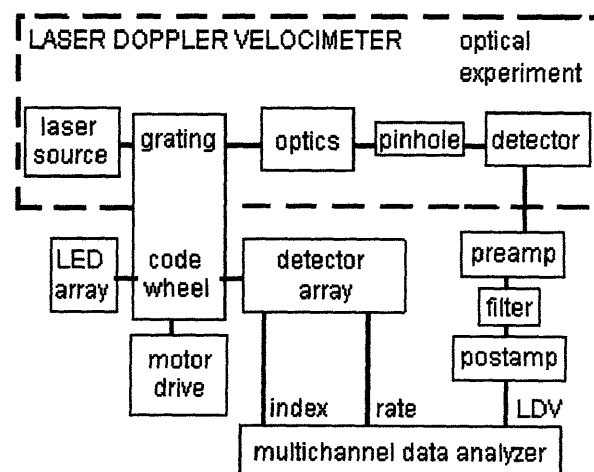


Figure 3-6. Experiment block diagram

OPTICAL EXPERIMENT -- RESULTS

Light from the HeNe laser source is directed to fall on the moving diffraction grating, and generate orders or secondary beams. Two of these orders are then routed via mirrors so that they may impinge, in parallel and phase-coherent, at the PIN photodiode detector. This allows the coherent components of the two secondary beam segments to interfere and produce a beat signal, as discussed above. This beat signal has a frequency which is directly proportional to the object's rotational velocity.

A small spot size is desirable at the grating surface. By keeping the source beam narrowly focused, the diffracted beams are similarly narrow, and very low operating power may be used. The use of tight focusing and a high degree of spatial selection, aside from being efficient, provides the best signal visibility or contrast, since a small target illumination area has a much better chance of maintaining phasefront planarity than an extended target area. Also, the beamsplitters and support optics are much easier to align given a small spot size.

Three philosophies were expressed relative to the use of lenses to focus the source beam onto the grating. First, it was thought that the addition of any lensing could have a deleterious effect on signal visibility. There would inevitably be fluctuations in phase planarity (via differential delays through the lens), and source lensing would dictate additional re-collimating lenses for the secondary beams (reflected from the target), since these beams would be beyond the focal point of the source lens and hence divergent. Second, if a focusing lens at the source were used, it seemed justified to select the object's rotation axis as the focal point, since this would make all incident rays normal to the disk edge, and each element of the surface illumination would appear as normal incidence on a locally flat grating. Third and finally, it was decided that the minimum spot size (beamwaist) at the grating would yield the least number of gratings illuminated, and hence the least curvature effects (divergence of the diffracted beams.) This suggested the placement of a thin lens in the source path, with a focal point on the target disk edge surface. Rather than individual recollimating lenses on each outgoing path, a single 'collecting lens' was used near the detector to refocus the beams.

The entire experiment was constructed on a standard optics laboratory bench (Newport Corp.), with compressed-air vibration-isolation mounts. Isolation was essential because the mirror and beamsplitter optics essentially comprise a Mach-Zehnder interferometer, which modulates the output beam depending on the difference in path length between the two arms of the interferometer (here the two paths from source to detector). Hence even small vibrations (of even a quarter of a wavelength or well under 1 micron) can cause unwanted amplitude modulation of the beat signals. These modulations would ordinarily swamp out the interesting signals.

POST-PROCESSING

The photodiode detector output was passed through a wideband pre-amp and then on to a low-frequency reject (high-pass) filter and post-amp before entering the acquisition and processing system. The Analogic (Data Precision) **DATA 6000A** analyzer system was employed to sample, manipulate, store, and analyze the detector output. Extensive use was made of the timebase, triggering, storage, FFT and correlation functions, and plotting capability of this system.

The next few pages contain sample runs of data collection with the optical experiments just described. The samples consist of an LDV detector output trace, the codewheel trace, the Fourier transform of the LDV signal, and a correlation plot of the recovered velocity as compared to the velocity derived from the reference codewheel. It will be seen that, once the radius correction due to the thickness of the grating (and its adhesive) is taken into account, the data are consistent with a zero-bias velocity estimator with an rms error of less than 0.5 % or so.

For a codewheel period of T , the expected doppler beat frequency is determined by:

$$v = \frac{2\pi \cdot R}{500 \cdot T} \qquad \Delta f_{\text{expected}} = \frac{2 \cdot v}{p}$$

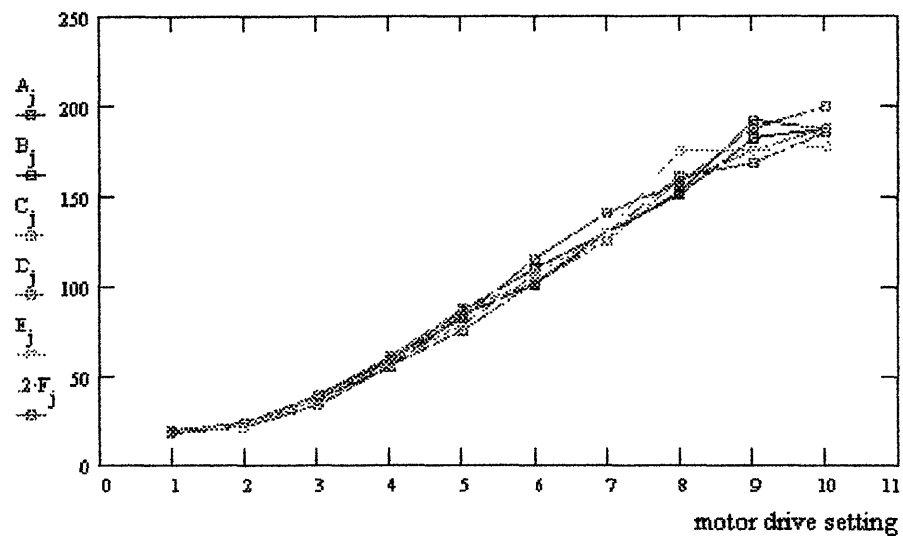


Figure 3-7 Linear motion: peak homodyne frequency vs. stepper motor setting

Samples A-E are glass grating (reference sample, $p = 10 \mu\text{m}$)

Sample F is Light Impressions "D1" grating ($p = 2 \mu\text{m}$)

[note: agreement achieved within limits of stepper drive repeatability]

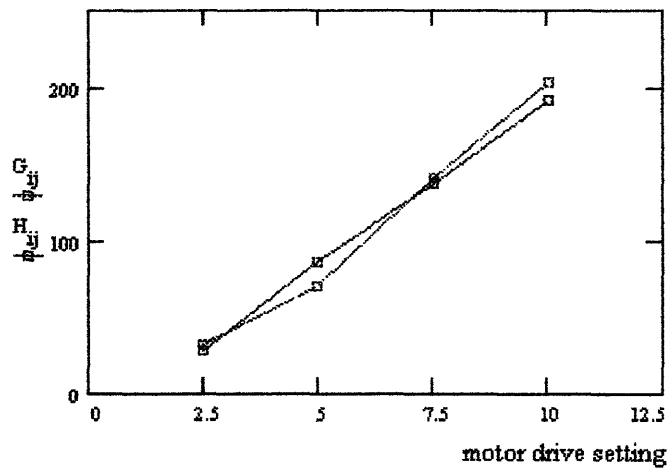


Figure 3-8. Linear motion vs. stepper motor setting

Samples G,H are Light Impressions grating "D1", $p = 2.0 \mu\text{m}$

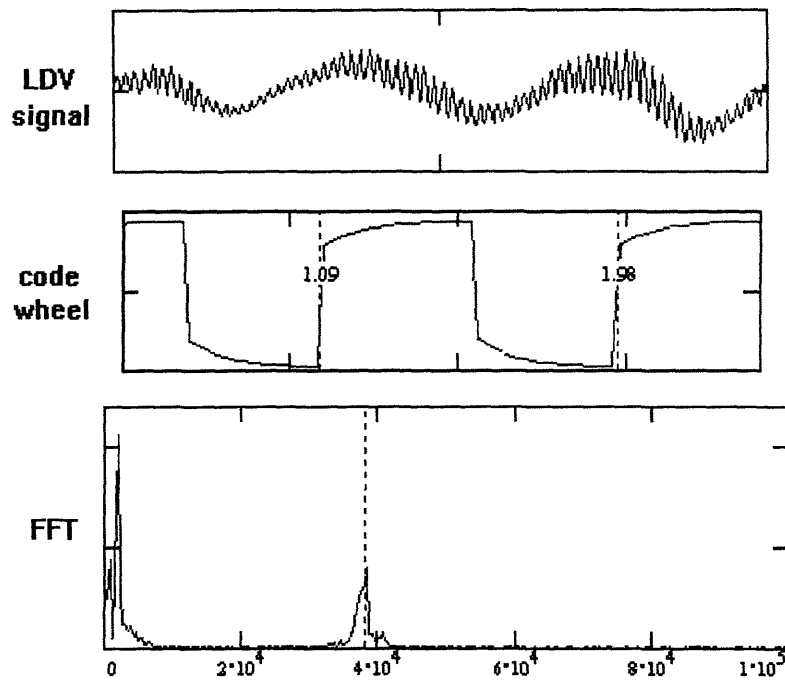


Figure 3-9. Sample traces of a.) LDV detector output voltage,
b.)codewheel squarewave at 500 cycles per revolution
c.) Fourier transform of (a.), with reference from (b.)

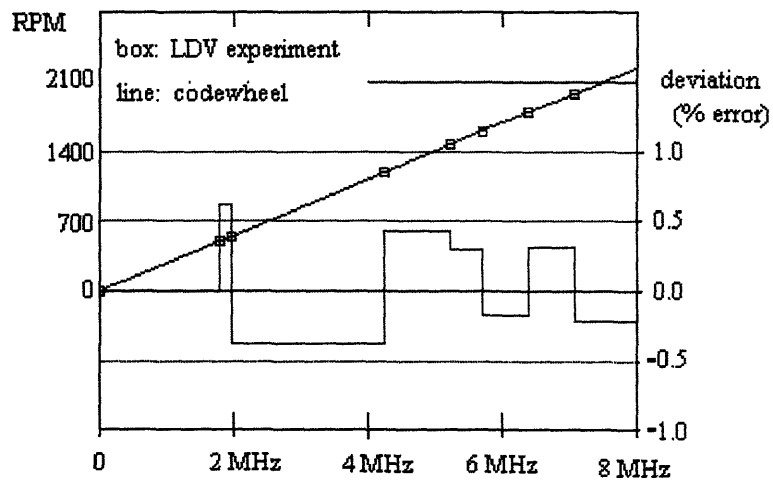


Figure 3-10) Rotary motion, R=0.5" disk

Light Impressions "Rainbow Box" grating, $p = 0.74$ microns

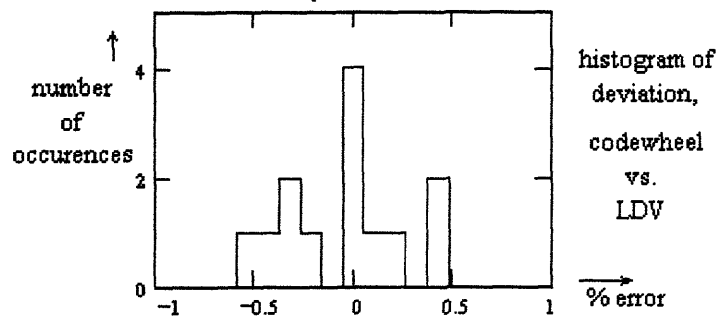
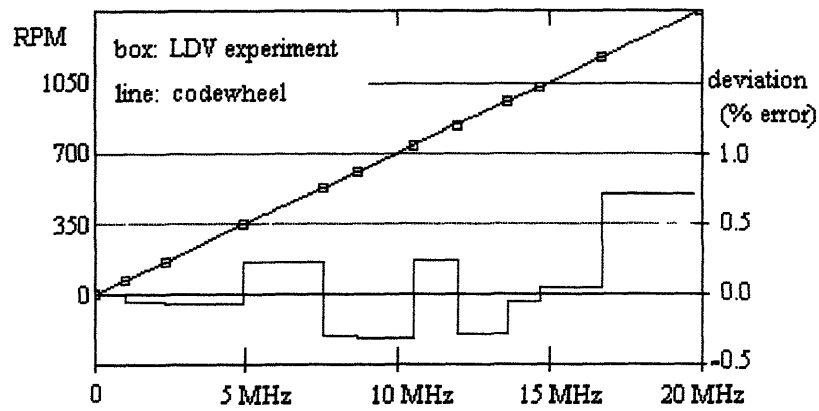


Figure 3-11) Rotary motion, $R = 2.0''$ disk

Light Impressions "Rainbow Box" grating, $p = 0.74$ microns

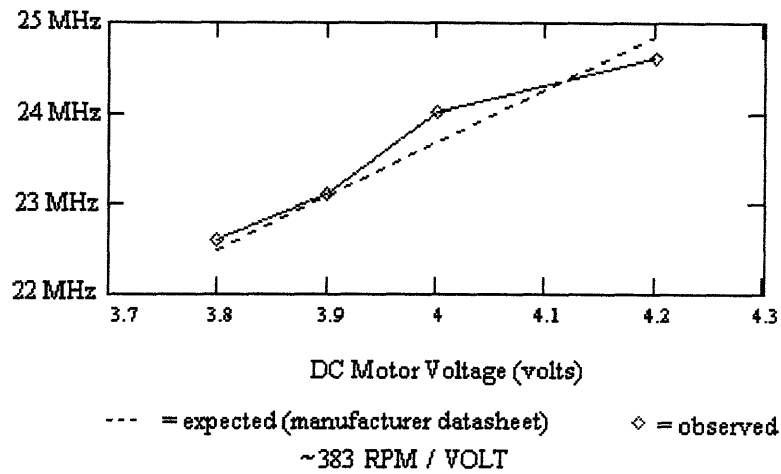


Figure 3-12) Doppler shift for high-speed rotation, R= 2.0" disk
vs. DC Motor datasheet voltage

[note: codewheel channel unavailable at maximum sampling rate]

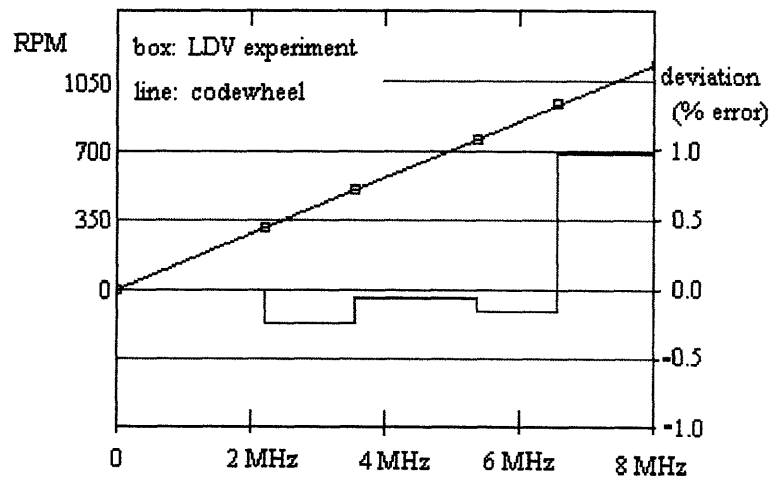


Figure 3-13) Rotary motion, R= 1.0" disk

Light Impressions "Rainbow Box" grating, p= 0.74 microns

4. DISCUSSION

In the coherent differential doppler velocimetry experiment the intensity and signal-to-noise ratio of the optical beat frequency, and hence the accuracy of any velocity estimates, depends on many factors. This section will consider the sources of error in the estimation, including source spatiotemporal coherence parameters, deviations due to geometry and imperfect optics, and detection and post-processing characteristics. We conclude with a survey of realized and potential applications in rotation and torsion sensing, with this and similar techniques.

"A clear understanding of the difference between temporal and spatial coherence, or between path-integrated frequency effects and differential phase changes across an aperture, helps one interpret the coherent differential Doppler technique." -- Schwiesow, et.al. [42]

We begin with a model of the final experimental configuration (Figure 4-1), and walk through the contributions to uncertainty in the velocity estimate.

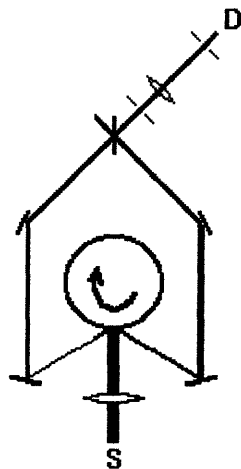


Figure 4-1. Coherent differential laser doppler velocimetry diagram
(coplanar layout)

The source is predominantly the fundamental Gaussian mode at its beamwaist. This source will have occasional bursts of other longitudinal and transverse modes, plus phase and polarization drift due to spontaneous emission, but these effects are very small. We choose for an initial model a singlemode Gaussian beam at 632.8 nm. wavelength, with minimum beamwaist w_0 of ~ 0.12 cm., and hence radius of curvature of $\frac{1}{R} = \frac{z}{z^2 + (\pi \cdot w_0^2 / \lambda)^2}$ or $\frac{1}{R} = \frac{z}{z^2 + 5.11 \cdot 10^5}$ for z in centimeters from the beamwaist (the total optical path length is ~ 40 cm.). The higher-order transverse Hermite Gaussian modes and their intensity *mode correlation functions* [12] are not explicitly considered here but will appear in the source phase modulation error term δS over the beam wavefront.

Additional longitudinal modes from the source, as inevitably occur in the HeNe laser, are expected to undergo the same doppler shift as the fundamental, but will diffract at an angular deviation of $\Delta\theta \cong \frac{m \cdot \Delta\lambda}{p} = 10^{-2}$ mrad, for the ± 1 mode for a 2 nm frequency offset. The angular size of the detector pinhole ($.35\mu$ diam) at the sensing distance (~ 40 cm) amounts to approx. $5 \cdot 10^{-4}$ mrad. Therefore these additional modes are spatially selected out. However, since these angles are very small and the uncertainties in the surface rather large, there is some risk of spectral contamination by the (longitudinal) mode-hopping of the laser. This effect is only 3 parts in 10,000 or so, and the intensity in these modes is already tens of dB down from the dominant. These modes could become worrisome at high sensed velocities (e.g. those leading to doppler shifts in excess of ~ 100 MHz.)

Temporally, the optical path lengths of the recombined beams are similar enough that the path difference (< 3 cm) is well within the coherence length of the laser (estimated at ~ 3 ns or length 30 cm). Therefore, there will be a very strong correlation between the phase and polarization states of the photons arriving at the detector from each beam, given a short enough detection sampling interval. Between the two beams, there will be the additional, symmetric doppler shift due to the moving grating (plus polarization and delay variations due to the intervening optics --see below.)

The lens used with the source to obtain a minimum spot size at the grating (that is, the beamwaist focused on the region of grating to be sensed), adds its own contribution to phase error via scattering and aberration. This also provides an opportunity for mode mixing, if local nonuniformities provide scattering centers that can couple energy to other propagation patterns. Considered statically, there will be non-uniform phase distortion (or differential delay) for the various spatial components within the beam. Characterization of the lens (and mirrors and beamsplitters) is summarized in a phase distortion specification (e.g., flat to $\lambda/10$), but the spatial distribution of such distortions is not well-specified, and must be gauged interferometrically [7, 20]. The positive results (high visibility) obtained suggest that local phase fluctuations were small.

TARGET SURFACE -- SPATIAL PREPARATION

Natural surfaces (such as the commercial-grade gratings used here) have imperfections and variable surface quality. Each surface element reflects a small portion of the incident light. The surface normals to these reflecting elements, if translated to a common origin, are distributed within a cone, a solid angle of spatial dispersion. Therefore the wavevectors of the reflected light will also become dispersed relative to the source. In addition to spatial 'loss' due to dispersion out of the *signal* path, there will also be momentum uncertainty due to angle mismatch in the source-grating- detector path, which scales the observed Doppler shift. Another way of stating this is that the additional spatial frequency components due to spatial irregularity of the grating contribute loss and broadening (temporal frequency uncertainty) when recovering the doppler beat signal spectrum.

General features of the rotation will exhibit themselves in the Doppler Fourier spectrum (see Fig 4-3b.) Eccentricity ($a/b \neq 1$) and non-concentricity ($c \neq 0$), shaft wobble ($\Delta x \neq 0$), and general large-scale surface roughness (Δr) will all have very strong components at the fundamental rotation rate - that is, one per full cycle of revolution. Of course seams, gaps, or other dropouts in the grating

as applied to the target will cause additional loss and extra low-frequency modulation. The spinning target object can also set up vibrations that acoustically couple to the sensing optics.

Any overall intensity profile, or 'image' as seen along the scanned surface, will provide the envelope within which all of the interference signals reside. The apparatus in essence is creating a real-time differential hologram [44](as contrasted with a reference-beam hologram) of the spinning surface. Therefore, the fringe envelope due to surface variations, imperfections and *speckle* (see below) will contribute signal energy in the low frequency spectrum. Fortunately, much of the surface roughness induced modulation occurs at low enough frequency to be filtered out for moderate observation speeds. Imperfections in the grating profile and spacing contribute additional direction (envelope) modulation, in broader frequency ranges.

The grating spatial bandwidth can be a useful grating quality measure, as it averages the very small scale imperfections and highlights large systemic biases like stretching or warping. In edge-based rotation observations, the curvature $1/R$ of the observed cylinder or disk translates to a set of spatial Fourier components near $2\pi/R$ and subharmonics. The diffraction orders coming off of a grating in this type of system have the initial source laser beam divergence plus an additional phasefront curvature of $1/R$.

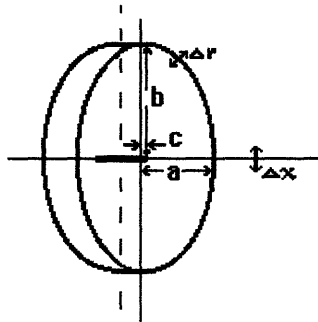


Fig 4-2a. Features of the rotation

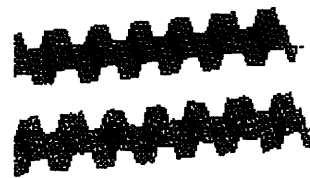


Fig. 4-2b. Ideal and non-ideal gratings

On a small scale (several wavelengths), local phase features in a material may cause "hot-spots" in the spatial reflection profile. This *speckle* phenomenon is most pronounced with singlemode

sources. This source of noise can be troublesome, since the discrete bursts generated as new speckle sources come into view may contain many frequency components. However, some researchers have made a virtue of necessity, extracting velocity estimates by spatially transforming the dynamic speckle pattern itself via an optical fiber array [29].

Precision etched diffraction gratings tend to be expensive. The inexpensive, mass-produced 'rainbow-effect' diffraction gratings on aluminized mylar as in the Light Impressions samples ("D1" and "Rainbow Box"), have other spatial frequencies present than a pure grating.

The possibilities for precision measurements in the ideal case, with a locally flat precision grating, certainly improve. It helps in this regard to have a very narrow beamwaist, strongly polarized beam centered on the grating. The field stop / receiver pinhole combination can be even more discriminating in terms of the spread of input vectors that will be accepted, since more power will be available in the information modes, without being lost to surface scattering. The fundamental accuracy of this 'ideal grating' case begins to be dominated by the source linewidth and modal stability performance, and the type of signal processing performed at the receiver.

Besides gratings, prisms also have great promise in providing the spatial selection and confinement necessary for the coherent techniques [7, 11]. But perhaps the problems of alignment are best avoided almost altogether by using the fiberoptic technique [8, 9]. It would appear that fibers are well able to maintain desirable coherence properties over the short distances required in this type of instrument [16, 26].

RECOMBINATION

The mirrors, beamsplitter, collection lens(es) and field stop provide the spatial selection and recombination for the two diffracted signal beams from the grating. The mirrors' reflection functions are relatively benign, but will contribute phase and polarization distortion if not of high quality. Similar remarks are in order for the beamsplitter. Any deviations from flatness of the reflecting planes will appear as additional phase modulation across the signal wavefront, and degrade the visibility of the desired beat signal. The collecting lens, which would be optional in a precision-grating experiment, allows a larger '*coherence area*' or *coherence zone* on an irregular target, since light beams from nearly-aligned positions can also be collected. This carries the penalty, though, of collecting other, shifted, scattered, or fringing fields from peripheral or undesirable paths, and as a result the visibility of the homodyne signal will suffer.

The mirrors and beamsplitter (and detector) may also have translational or vibrational drift or oscillation that can cause additional doppler shifts with respect to the original laser center frequency. In the somewhat extended bench setup used, these vibrations can be problematic. Miniaturization and integration with optical fibers (discussed below) should virtually eliminate the optics-vibration component of the velocity estimate error.

The combination of the field stop, (precision) pinhole, and detector surface coating provides the final spatial selection on the recombined beams. The pinhole size is selected to minimize the size of the zone where coherence must be maintained. That is, the pinhole diameter should be less than the full fringe width caused by the non-parallel beams arriving from the beamsplitter. Of course the pinhole must allow sufficient power through to the detector for a healthy SNR. The pinhole is mounted flush to the detector surface to avoid any extra diffraction effects. When using the H-P HFBR photodetector/preamp, no pinhole was needed (this detector is designed for use with optical fibers with a typical spot size of 50 microns width, accomplished via a very small active area detector and a receiving lens.)

SUMMARY UNCERTAINTY MODEL

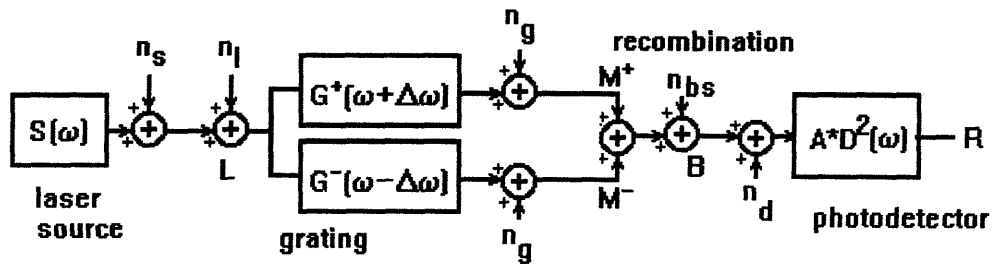


Figure 4-3. Sources of noise and uncertainty in the coherent differential doppler velocity measurement

The combined phase (and phase rate) distortion effects of the coherent differential system optics may be represented by Figure 4-3 above. For each process, source, lens, grating, ..., there is an associated phasefront perturbation δS , δL , δG .

In the experiments performed, the grating contribution δG outweighed all others. Prior to vibration isolation, the lens, mirror, and beamsplitter factors δL , δM , and δBS were significant. In experiments with higher-quality gratings and mechanical stability, the source term δS is expected to predominate.

For reference purposes, the equivalent uncertainty model for the light chopper codewheel system is shown in Figure 4-4 below. The fundamental resolution is much coarser, and so the perturbations are of lesser relative magnitude.

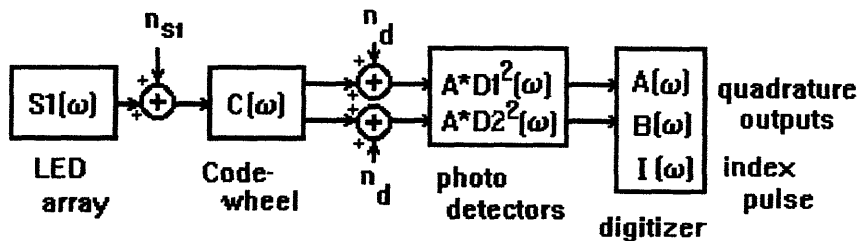


Figure 4-4. Codewheel (reference) velocity estimator uncertainties

DETECTION

The photodiode detector used in these experiments provides a photocurrent, as described in Section 2, that is proportional to the incident intensity at the detector surface. The visibility of even a perfect optical beat signal will be limited by the detector shot noise, which in effect produces a wideband background current. The shot noise induced current is of a density consistent with an optical *noise equivalent power* (NEP) of, typically, about -43 dBm ($\sim 0.05 \mu\text{W}$) for a silicon or germanium photodiode detector. The photocurrent is then typically amplified by a transimpedance amp and other gain stages and filters.

More sensitive detectors can operate with lower input power (high gain) and lower noise (NEP better than -60dBm) with photomultiplier tubes (PMTs) or solid-state avalanche photodiodes (APDs.) These detectors can in fact detect down to the single-photon level, and hence are used in photon counting receivers. New techniques such as "active quenching" overcome the long dead-times associated with resetting the APD for reacquisition (this technique actively modulates the bias to the APD diode to obtain faster recovery after an event is detected.) Photons can now be counted at up to $\sim 40,000$ per second per APD detector [8].

PROCESSING -- BURST ANALYSIS

Given the surface roughness, motions, and irregularities discussed above, a velocimeter probe experiences intermittent intervals when the diffraction lines up with the beamsplitter and detector. Therefore the detector sees bursts of signal when sufficient energy comes through into alignment. The width of such a burst may be called a 'dwell time' τ within the coherence area. A pure sine wave modulated by a Gaussian shaped temporal burst of full width half maximum τ yields after Fourier transforming a Gaussian shaped pulse, centered at the sinusoidal frequency and spread over a spectral width of $2\pi / \tau$. Thus it is immediately seen that to obtain a sinusoid's frequency with absolute accuracy requires an infinite sampling interval. In general, the accuracy of the velocity estimate will improve as more cycles are accumulated and averaged.

However, to very good accuracy, the frequency may be obtained by a number of techniques. The first task is to obtain a 'trigger' when the coherence area comes into alignment and the optical beat signal falls on the detector. This is known as 'amplitude-conditioned sampling' [30]. The sampled modulated tone bursts can then be passed through a filter to discriminate their frequency. The filter might be implemented as a wideband PLL or thresholding trigger that tracks the bursts themselves and their envelope, followed by a narrowband loop to track frequency within the burst. With quasi-analog processing, the zero-crossings intervals of the ac-coupled sense data are digitized and FIR filtered [8].

There are also a wide variety of digital and 'pseudo-analog' processing approaches to the burst analysis problem. The most obvious digital technique is the FFT (Fast Fourier Transform) processing algorithm, which has been shown to perform well in this task [3]. The key to the accuracy of laser doppler rotation sensing is the ability to extract the peak frequency in the intensity power spectrum observed. In practice, the peak frequency f_{pk} can be determined to a much better accuracy than the full width half maximum value Δf [39]. The peak can be extracted, for example, by a bank of digital bandpass filters and some post-processing involving spline fitting [40]. For both analog and digital methods, however, there exist fundamental averaging time constants and acquisition and tracking bandwidths that limit the ultimate resolution and accuracy.

With photon counting, the photocount rate is proportional to the intensity. The autocorrelation of the photon arrival time is plotted in a "correlogram", and its Fourier transform effectively extracts the velocity estimate [8]. A recent paper suggests that the two-photon "time interval probability", rather than the standard intensity correlation approach, provides a higher overall accuracy, especially when low-intensity light beams are used [3].

TORSIONAL STRESS SENSING AND ANALYSIS

If two or more gratings (or a continuous band) are applied to a rotating object, separated by some distance along the rotation axis, then independent measurements of the rotational velocity will not necessarily agree precisely. In addition to noise differences, there will also be the real difference due to the fact that, instantaneously, the various sections of the rotating object may not all be spinning at the same rate. In a car axle, for example, torques applied via the drive shaft induce twisting of the axle (torsional deformation.) In this regard, even highly dense and stable materials undergo elastic 'torsional modes' [27, 36, 38]. Typically, these modes will appear as offsets of the relative angular position(s) of the two (or more) sections sensed. Twisting forces or torques applied to the system will generate (damped) oscillations of the angular displacements.

Each disk cross-sectional element of the spinning object under study behaves according to the following second order model [9]

$$J \cdot \Omega'' + D \cdot \Omega' + K \cdot \Omega = \bar{F} \quad (4-2)$$

with Ω as the angular phase (the integral of angular velocity), J summarizing the moments of inertia, D the damping coefficient, K the spring constant, and \bar{F} representing the driving force or torque. This model permits both overdamped (stable) and underdamped (chaotic or oscillatory) harmonic variations. The absolute phase Ω does not always return to zero but may have a static twisting offset due to the applied torque. Therefore, for torque and torque-loss experiments, absolute (phase) encoding is desirable. Also, in developing the phase-space trajectories of the motion, continuous recording and integration are necessary.

Torsional modes can be investigated by extending the optical experiment to provide two (or more) sensing channels, referenced to the same optical source, and separated by an adjustable distance along the target's rotation axis. Alternatively, the entire LDV device can be scanned back and forth along a line segment parallel to the rotation axis [43]. In this way, an *axial transverse velocity profile* can be developed along the sensing line.

Cairolì et. al. [9] suggest that torsional properties may be assessed at a single sampling point along the object's axis. Via the "peripheral velocity fluctuations" method, an estimate of the elasticity and damping of the cross-sectional disk element may be obtained.

One straightforward processing approach for torsion sensing using two LDV probes utilizes a (rf) mixer to combine the two beat frequencies from the two (offset) sensors to form a difference frequency. This difference frequency is a direct observation of the torsional phase rate between the two observation points. Note that this is a rate measurement and does not yield absolute strain or torque. Once again, the sensitivity of the measurement will be limited by practical considerations of alignment, surface uniformity, vibration, etc. The difference signal between the two velocity measurements may be quite small, and hence noise dominated, for low levels of applied torque. In this instance, a frequency shift or heterodyne approach may be warranted. The presence of dropouts in one or both sensor signals is a further complication that would have to be dealt with via signal conditioning or output gating, as in the 'amplitude conditioned processing' described above.

PRODUCT DEVELOPMENT

Successful introduction of sensing devices based on this technique will be determined by the cost, reliability, sensitivity, and usefulness of the implementation. Certainly, a new device would have to be compatible with existing practices in the respective application disciplines; such as vehicular development or testing, power generation, or aerospace.

The flexibility and application domain of LDV devices would be much aided by miniaturization. Aside from cost reduction; the use of semiconductor laser diode sources, integrated optics (fibers, microlenses, ...) APD receivers, and the like would result in much more compact and stable instruments, which could then be coupled to pc interfaces for a variety of standard or custom hardware-assisted processing options.

"Laser diodes may replace gas lasers, optical fibers and microlenses may replace bulkier optical systems, single photon counting avalanche photodiodes may replace photo-multipliers, and software and/or semicustom electronic cards may replace hard wired boxes of correlation electronics, ..."
-- Brown, et.al. [8]

The uncertainty analysis for the 'miniaturized' version proceeds as before, with polarization-preserving fiber paths and couplers replacing the mirror-beamsplitter-collecting lens arrangement. A detailed investigation of the modes excited within the fibers would be worthwhile to understand the spatial confinement achieved, and hence the expected measurement accuracy. Microlenses may be required in some instances.

SUMMARY

Rotations and torsional modes of a spinning object are investigated by means of a coherent light source incident on a diffraction grating. The grating may be applied to the surface exterior (for example as an adhesive label) or etched into the surface of the material to be sensed [46]. It is conceivable that this method could be used with the natural speckle pattern of the surface being scanned, as in electronic speckle pattern interferometry (ESPI) [47]. However, we have obtained promising results with simple, inexpensive, adhesive-backed commercial gratings.

Theoretical and practical limitations of various experimental configurations have been evaluated. The theoretical or ideal experiment is mainly determined by source characteristics, such as source coherence time/length, stationarity (modal stability) and beam profile and divergence. Also, the reflectivities and phase factors of the grating, recombining optics, and the detector characteristics are of prime importance in practical implementations.

Maintaining phase coherence throughout the experiment is the primary challenge. In particular, the beams incident on the detector must be very nearly parallel. Practical limitations on the experiment also include general alignment issues, including surface roughness / flatness, grating

non-uniformity, target curvature, and target eccentricity, vibration, or radial play. In our testbed, the motor drive itself presented load and velocity fluctuations, as well as electrical noise.

Detector noise and active area uniformity contribute additional uncertainty. The real-time acquisition delay and tracking error will depend on the PLL (or other) design utilized. Acquisition bandwidth and I/O throughput will be important behavioral parameters. Due to surface characteristics, there will be occasional 'fades' of the signal. Therefore the velocity sensed will have intermittent dropouts and varying SNR. A practical sensing instrument will have to accommodate these features.

For a known grating, the angles of the primary (± 1) diffraction orders is precisely determined. However, the distance of the sensing head from the grating, and hence the correct alignment of the receiving optics for each recovered order, is unknown. If a mounting or reference surface is available which is stable with respect to the spinning surface being sensed (e.g., a shaft housing or flange), this is not a problem. When the sensing head does not have a stable platform, or if the spinning object has a large amount of axial play or wobble, a mechanism for tracking and compensating the probe-head to target distance (i.e. a distance servomechanism) may be required. Mechanisms similar to this one have been implemented in CD drives, for example.

For torsional stress sensing, the following limitations also need to be considered: low frequency noise, mechanical stability of the splitting and recombining optics (e.g., vibration isolation), and stability of the sensor separation distance. Scanning approaches that use piezoelectric steering mirrors, acousto-optic devices, or synthetic apertures are also possible, and could yield a velocity profile and/or a torsional stress profile along a segment parallel to the spinning object's axis of rotation.

With an extremely precise rotational velocimeter, unknown details of the structural mechanics of spinning mechanical systems can be revealed. With simple, inexpensive gratings, a high level of accuracy is achievable. With integrated optics, optical fibers, solid-state lasers and new detector designs, together with advanced signal processing techniques, a flexible, portable and relatively inexpensive instrument can be developed which will compete favorably with present rotary encoder techniques that require the presence of a codewheel. In the differential coherent laser doppler velocimeter, only the laser beam (and grating) touches the object to be sensed.

REFERENCES / BIBLIOGRAPHY

- [1] Kh. T. Abeinayake, V. A. Komotskii, and M. V. Kotyukov, "Measurement of Velocity of Surface Acoustic Waves by Optical Probing Method with Reference Diffraction Grating", *Avtometriya*, No. 1, pp. 97-100, 1989.
- [2] R. J. Adrian, "A Bipolar, Two Component Laser-Doppler Velocimeter", *J. Phys. E* 8, 723 (1975).
- [3] J. M. Alvarez, M. A. Rebolledo, and J. Tornos, "Comparison between intensity correlation and Fourier transform of the time interval probability techniques applied to laser Doppler velocimetry", *Applied Optics*, Vol. 28, No. 17, 1 September 1989, p. 3662.
- [4] E. A. Ballik and J. H. C. Chan, "SNR in optical velocimeters: effect of detection angle", *Applied Optics*, Vol. 16, No. 3, March 1977, p. 674.
- [5] P. Ya. Belousev, Yu.N. Dubnitshev, and V. G. Meledin, "Optical velocimeters for moving surfaces using gas and semiconductor lasers", *Optics and Laser Technology*, Vol. 22, No. 5, 1990, p. 335.
- [6] P. Ya. Belousev and Yu.N. Dubnitshev, "The application of an optical Doppler frequency discriminator in a laser velocimeter", *Optics and Laser Technology*, October, 1977, p. 229.
- [7] M. Born and E. Wolf, "Principles of Optics", Pergamon Press, New York, 1980.
- [8] R. G. W. Brown and E. R. Pike, "A combined laser doppler and time of flight anemometer", *Optics and Laser Technology*, December 1978, p. 317.
- [9] M. Cairoli and M. Martinelli, "All-Fiber Reference-Beam LDV-Probe for In-Field Shafts Torsional Monitoring", *SPIE Vol. 1012 In-Process Optical Measurements*, 1988.
- [10] M. Dahleh, R. Nevels, and L. Tsang, "Plane-wave diffraction by a dielectric-coated corrugated surface", *J. Appl. Phys.*, Vol. 58, No. 2, 15 July 1985, p. 646.
- [11] L. E. Drain, "The Laser Doppler Technique", John Wiley & Sons, London, 1980.
- [12] K. M. Du, G. Herziger, P. Loosen, and F. Ruhl, "Coherence and intensity moments of laser light", *Optical and Quantum Electronics*, Vol. 24, June 1992, p. S1081.
- [12a] K. M. Du, G. Herziger, P. Loosen, and F. Ruhl, "Computation of the statistical properties of laser light", *Optical and Quantum Electronics*, Vol. 24, June 1992, p. S1095.
- [13] Yu. N. Dubnistchev and Yu. G. Vasilenko, "A laser Doppler velocimeter which measures the three components of velocity", *Optics and Laser Technology*, June 1976, p. 129.
- [14] Edmund Scientific Company, Barrington, NJ, "1992 Annual Reference Catalog for Optics, Science and Education", #12N7.
- [15] T. Eiju and K. Matsuda, "Determination of the central position of rotation of rotating object by laser Doppler velocimetry", *Optical Engineering*, Vol. 30, No. 11, November 1991, p. 1825.
- [16] A. R. Evseev and V. A. Orlov, "Differential Doppler Velocity Meter with Fiber Waveguides", *Avtometriya*, No. 6, pp. 62-68, 1986.
- [17] R. P. Feynman, "QED; The Strange Theory of Light and Matter", Princeton Science Library, Princeton, N.J., 1985.

- [17a] L. M. Fingerson, "Laser Doppler Velocimeters", *Fiberoptic Technology*, August 1982, p. 53.
- [18] R. J. Glauber, "Coherence and Quantum Detection", from lectures delivered at Harvard University.
- [19] H. Haken, "Light: Laser Light Dynamics", North Holland, Amsterdam, 1985.
- [20] H. A. Haus, "Waves and Fields in Optoelectronics", Prentice-Hall Inc., Englewood Cliffs, NJ, 1984.
- [21] Dr. Johannes Heidenhain GmbH, Traunreut, Germany, "Rotary Encoders", product catalog #20872021, August 1993.
- [22] Hewlett-Packard Components Group, "Optoelectronics Designer's Catalog", 1991-1992 databook
- [23] H. H. Hopkins, "The Theory of Coherence and Its Applications", Chapter VI in "Advanced Optical Techniques", edited by A. C. S. Van Heel, John Wiley & Sons, New York, 1967.
- [24] S. L. Huang, "Metrological grating technology developments", SPIE Vol. 815 Application and Theory of Periodic Structures, Diffraction Gratings, and Moire Phenomena III (1987), p. 174.
- [25] A. R. Hunter and T. M. Morton, "Application of Holographic Interferometry to Predict Long-time Torsional Relaxation", *Experimental Mechanics*, April 1975, p. 153.
- [26] M. Imai and Y. Ohtsuka, "Spatial coherence of laser light propagating in an optical fibre", *Optical and Quantum Electronics*, Vol. 14, February 1982, p. 515.
- [27] J. O. Kim and H. H. Bau, "Torsional Stress Waves in a Circular Cylinder with a Modulated Surface", *Journal of Applied Mechanics*, Vol. 58, September 1991, p. 710.
- [28] P. W. Kinman and R. M. Gagliardi, "Doppler and range determination for deep space vehicles using active optical transponders", *Applied Optics*, Vol. 27, No. 21, 1 November 1988
- [29] Y. Kitagawa and A. Hayashi, "Fiber-optic sensor for distance and velocity measurements using speckle dynamics", *Applied Optics*, Vol. 24 No. 7, 1 April 1985
- [30] L. Lading and R. V. Edwards, "Laser Velocimeters: lower limits to uncertainty", *Applied Optics*, Vol. 32, No. 21, 20 July 1993, p. 3855.
- [31] S. W. Li and T. Aruga, "Transmission-grating velocimetric technique for common objects", *Applied Optics*, Vol. 31, No. 4, 1 February 1992, p. 560.
- [32] R. Loudon, "The Quantum Theory of Light", Oxford University Press, Oxford, 1973.
- [33] Lucas Control Systems Products Division, Vandalia, Ohio, "Ledex Incremental and Absolute Rotary Encoders", product catalog #LL-9111, 11/92.
- [34] J. H. Mauldin, "Light, Lasers, and Optics", TAB Books, Blue Ridge Summit, PA, 1988.
- [35] A. Mooradian, "Laser Linewidth", *Physics Today*, May 1985, p. 43.
- [36] K. W. Neale and S. C. Shrivastava, "Analytical Solutions for Circular Bars Subjected to Large Strain Plastic Torsion", *Transactions of the ASME, Journal of Applied Mechanics*, Vol. 57, June 1990, p. 298.
- [37] J. Oldengarm, "Development of rotating diffraction gratings and their use in laser anemometry", *Optics and Laser Technology*, April 1977, p. 69.

- [38] M. O'Rourke and T. F. Zebrowski, "Lower Bound for Fundamental Torsional Frequencies", *Journal of Applied Mechanics*, September 1976, p. 510.
- [39] D. P. Robinson, "Approximate models for the analysis of laser velocimetry correlation functions", *Optics and Laser Technology*, April 1981, p. 85.
- [40] A. E. Savakis, J. W. Stoughton, and S. V. Kanetkar, "Spline Function Approximation for Velocimeter Doppler Frequency Measurement", *IEEE Transactions on Instrumentation and Measurement*, Vol. 38, No. 4, August 1989, p. 892.
- [41] F. Schneider and W. Windeln, "Three-dimensional Doppler anemometer using a holographic optical element", *Applied Optics*, Vol. 27, No. 21, 1 November 1988
- [42] R. L. Schwiesow, R. E. Cupp, M. J. Post, and R. F. Calfee, "Coherent differential Doppler measurements of transverse velocity at a remote point", *Applied Optics* Vol. 16 No. 5, May 1977.
- [43] P. Sriram, S. Hanagud, J. Craig, and N. M. Komerath, "Scanning laser Doppler Technique for velocity profile sensing on a moving surface", *Applied Optics*, Vol. 29, No. 16, 1 June 1990, p. 2409.
- [44] G. W. Stroke, "An Introduction to Coherent Optics and Holography", Academic Press, London, 1969.
- [45] D.F. Wallis, "A Simple Field Theoretic Description of Photon Interference", reprinted in P.L Knight and L. Allen, "Concepts of Quantum Optics", Pergamon Press, Oxford, 1983.
- [45a] D. Wallis and G. Milburn, "Quantum Optics", Springer-Verlag, New York, 1994.
- [46] P. Wileman et. al., "The Laser Strain Gauge: Micro machining of diffraction gratings using an Excimer laser", *Strain*, February 1994
- [47] C. Wykes and M. Flanagan, "The use of a diode laser in an ESPI system", *Optics and Laser Technology*, Vol. 19, No. 1, Feb. 1987, p. 37.

Acknowledgements

The author would like to gratefully acknowledge the extreme patience and understanding of his advisor, Professor George W. Pratt, Jr. For useful discussions of experimental techniques I thank visiting scientist Dr. Krikor Bezjian, Professor Hermann Haus, and Todd Farrington. For machining support I am most grateful to Steven Farrington of Framingham, Mass. Dave Foley of Hewlett-Packard, Kevin Sampson of Light Impressions, Inc., Lian Shaw of American Holographic, Inc., and Jeremy Lerner of Physical Optics Corp. provided valuable information and samples. Brian Susnock contributed a thoughtful review of the manuscript. The Center for Material Science and Engineering laboratory and facilities management, and chemical and laser safety officers are also to be acknowledged.

Additional supporting thanks goes to chief administrator Anne Hunter in the Course VI undergraduate / M. Eng. office, secretary Connie Fazio, Dan Langdale in Student Financial Aid, and Liz Barnes and Mary Stewart in the Bursar's Office. Of course none of this would have been possible without the support of my parents and my sister Daryl.

The manuscript was prepared and edited in Microsoft MS-Word(TM) version 2.0. Mathematical processing was performed via Mathsoft, Inc.'s MathCAD PLUS(TM) revision 5.0+.

APPENDIX A

The following appendix contains a series of MathCAD(TM) simulations of the patterns observed from diffraction gratings of various shapes, sizes, configurations, and illuminations. Initially, and for reference cross-checking purposes, the Huygens-Fresnel sum of contributions from all point scatterers is used. Later, Fourier methods are applied (see Section 2- Diffraction grating theory in the main body of the text.) In the first section it is demonstrated that the Huygens-Fresnel sum sometimes requires more than 1000 points per facet (line pair) to begin to faithfully reproduce the pattern obtained with the Fourier method.

In particular, this appendix highlights the variations in reflected intensity from diffraction gratings of 3 kinds (3 different grating periods, $p = 10\text{ }\mu\text{m}$, $2\text{ }\mu\text{m}$, and $0.74\text{ }\mu\text{m}$), in flat and curved configurations, with uniform and Gaussian illuminations. The observation screen location and curvature are varied as well. The effect of line spacing (spatial period), curvature, duty cycle (reflectivity profile of grating line pairs), and spatial irregularity (noise) are considered and graphically depicted.

Diffraction grating study, via Mathsoft, Inc. MathCAD 5.0+

Fixed parameters of the simulation

Laser Source

incidence: $\vec{-z}$

HeNe laser wavelength: $\lambda = .6328 \cdot 10^{-4} \cdot \text{cm}$ $k = \frac{2 \cdot \pi}{\lambda}$

beamwaist: $w_0 = .12 \cdot \text{cm}$

illumination (Gaussian fundamental mode):

scaling $\mu = 10^4 \cdot \text{cm}^{-1}$ $\chi = \text{cm}^{-1}$

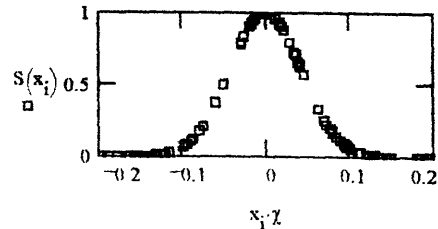
$u_m = 10^{-4} \cdot \text{cm}$

$N = 100$

$i = 0..N - 1$

$x_i = (\text{rnd}(.4) - .2) \cdot \text{cm}$

$S(x) = e^{-\left(\frac{2 \cdot x}{w_0}\right)^2}$



Diffraction Grating --

Reflectivity: 1.0, all surfaces presumed perfectly reflecting

Grating configuration parameters:

Spatial period: $\Lambda = 1/\text{cm}$

Source illumination spatial profile S: (central) coordinates x, z or $r, 0$

Observer surface-- **Grating curvature:**

$\text{rdisk} = \begin{pmatrix} 1.625 \\ 2.54 \\ 5.08 \end{pmatrix} \cdot \text{cm}$ 1" disk, 2" disk, 4" disk

Observer surface parameters

Observer detection surface P: coordinates X, Z or R, θ

Reflection mode intensity distribution I: $I(P)$

COMPUTATIONS of the field at the observer point

Distance

$$D(x, z, X, Z) = \sqrt{(x - X)^2 + (z - Z)^2}$$

Fresnel-Huygens (N surfaces, M points each)

$$E1(P) = \sum_{i=1}^N \sum_{S=1}^M e^{j \cdot k \cdot D(S, P)} e^{j \cdot k \cdot (\max(z_S) - z_S)}$$

Square pulse transform

$$\text{sinc}(\tan \theta, a) = \frac{\sin\left(\pi \cdot \tan \theta \cdot \frac{a}{\lambda}\right)}{\left(\pi \cdot \tan \theta \cdot \frac{\text{cm}}{\lambda}\right)}$$

Fourier (N surfaces S_i)

$$E3(P) = \sum_{i=1}^N e^{j \cdot k \cdot D(S_i, P)} \int_{S_i} S e^{j \cdot \vec{k} \cdot \vec{x}} dx$$

1: Test Case, single rectangular illumination (one grating)

grating elements illuminated: $N = 1$

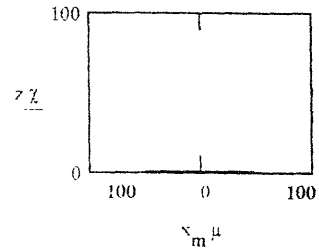
rectangle width: $a = 100 \cdot 10^{-4} \text{ cm}$ 100 micron aperture

#points across rectangle: $M = 1000$ $m = 0, M-1$

illumination coordinates: $z = 0 \cdot \text{cm}$ $x_m = a \cdot \frac{(m-1)}{M-2}$

#points across observer screen: $P = 100$ $p = 0, P-1$

Observer screen (flat) $z_p = 1 \text{ cm}$ $X_p = \frac{p}{P} \cdot 0.3 \cdot \text{cm}$



Field at observer (Huygens)

$$E1_p = \sum_{m=0}^{M-1} e^{j k D(x_m, z_p, X_p, Z_p)}$$

Intensity at observer $I1_p = \frac{(|E1_p|)^2}{(|E1_0|)^2}$

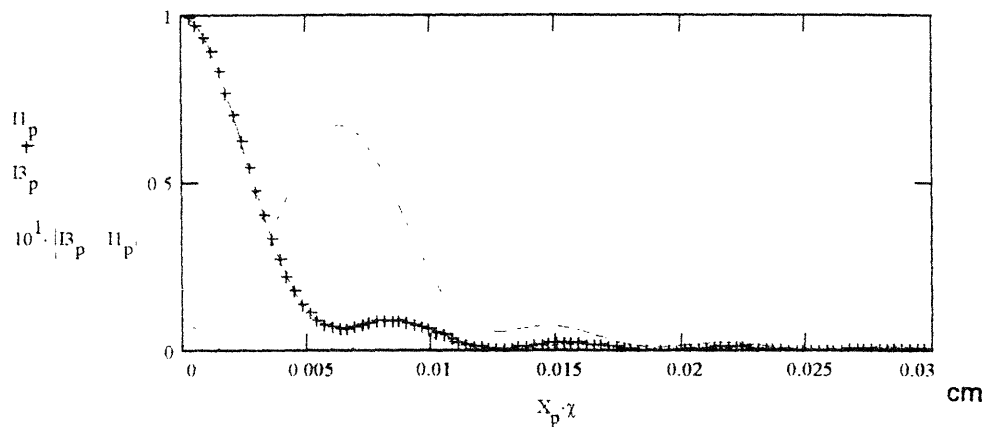
$$DM_p = D\left(\frac{M-1}{2}, z_p, X_p, Z_p\right)$$

Fourier

$$E3_p = \sum_{n=1}^N e^{j k DM_p} \frac{\sin\left(\pi \frac{X_p - a}{DM_p \lambda}\right)}{\pi \frac{X_p - a}{DM_p \lambda}}$$

$$I3_0 = 1$$

$$I3_p = \frac{(|E3_p|)^2}{(|E3_1|)^2}$$



2: Test Case, single rectangular illumination (one grating), inclined

grating elements illuminated: $N = 1$ width: $a = 2 \cdot 10^{-4} \cdot \text{cm}$

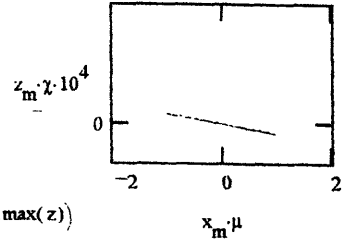
#points across rectangle: $M = 1000$ $m = 0..M-1$

illumination coordinates: $h = 1.5 \mu\text{m}$ max height

$$z_m = h \cdot \left(\frac{m}{M} - \frac{1}{2} \right) \quad x_m = a \cdot \left(\frac{m}{M} - \frac{1}{2} \right)$$

#points across observer screen: $P = 200$ $p = 0..P-1$

Observer screen (flat): $Z_p = 1 \text{ cm}$ $X_p = \frac{p}{P} \cdot 2 \cdot \text{cm}$



Field at
observer
(Huygens)

$$E1_p = \sum_{m=0}^{M-1} e^{j \cdot k \cdot D(x_m, z_m, X_p, Z_p)} \cdot e^{j \cdot k \cdot D(0, z_m, 0, \max(z))}$$

$$MM = \frac{M}{2} - 1 \quad DM_p = D(x_{MM}, z_{MM}, X_p, Z_p)$$

Intensity
at observer $I1_p = (|E1_p|)^2$
 $\max1 = \max(I1)$

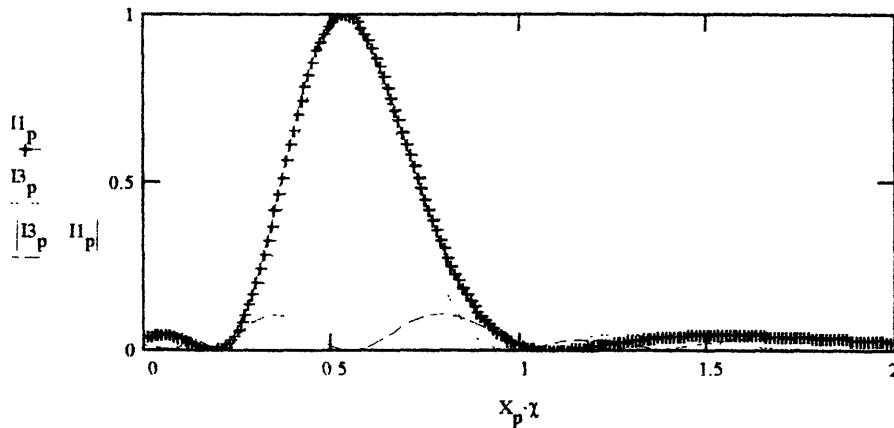
Fourier

$$E3B_p = \sum_{n=1}^N e^{j \cdot k \cdot DM_p} \cdot \text{sinc} \left(\frac{X_p \cdot \left[\frac{z_0}{x_0} \right] \cdot 2.15 \cdot Z_0}{DM_p}, a \right)$$

$$I1_p = \frac{I1_p}{\max1}$$

normalize

$$I3_p = \frac{(|E3B_p|)^2}{\max3} \quad \max3 = \max(I3) \quad I3_p = \frac{I3_p}{\max3}$$



Define a source: HeNe laser $\lambda := 632.8 \cdot 10^{-9}$

Wave analyzer -- agb 11/20/94

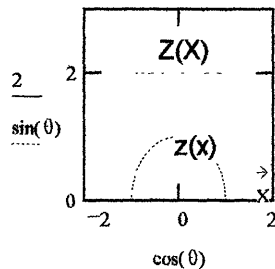
Illumination is uniform planewave,
propagating in -z direction

$$k = \frac{2 \cdot \pi}{\lambda}$$

beam waist(FWHM)= 2 mm

$$w = 2 \cdot 10^{-3}$$

$$\theta := 0, 1 \dots 2 \cdot \pi$$



Target: Diffraction grating
- point scatterers

$$p := 2 \cdot 10^{-6}$$

grating period

$$N_g = \frac{w}{p}$$

#gratings
illuminated
 $N_g = 1 \cdot 10^3$

For quick plots:

$$N_g := 40$$

DEFINE Target surface specification $z(x_m)$ = Height z of m scatterers at locations x_m
scale parameter $R := 10^{-2}$ 1 cm

HORIZONTAL x:

m points illuminated
uniform separation

$$m := 0 \dots N_g$$

$$x_m = -\frac{N_g}{2} \cdot p + p \cdot m$$

VERTICAL z: flat grating at z= R

$$z_m := \text{if}(x_m < 0, R, R)$$

DEFINE Image surface specification Z_n = Height Z of n locations at which to
(projection screen) observe field intensities, at coordinate X_n

HORIZONTAL X: N points calculated
(resolution)

$$N := 400$$

$$n := 0 \dots N$$

flat, +/- Xmax
uniform, symmetric

$$X_{\max} := 4 \cdot R$$

$$X_n := X_{\max} + \frac{n}{N} \cdot 2 \cdot X_{\max}$$

VERTICAL Z: Flat screen, $Z(X)=2R$

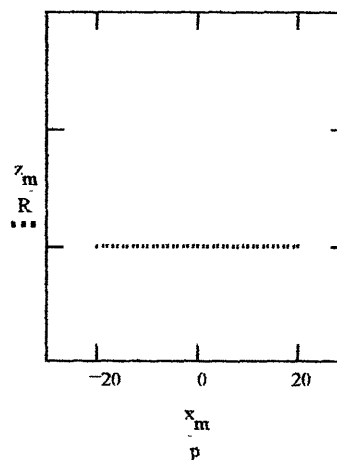
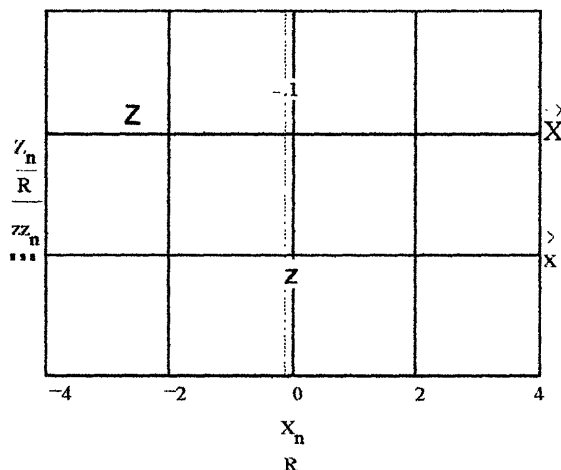
target outline on image screen

$$Z_n := \text{if}(X_n, 2 \cdot R, 2 \cdot R)$$

$$ZZ_n := \text{if}\left(\left|n - \frac{N}{2}\right| < b, 1, 0\right)$$

TARGET AND IMAGE Surfaces

Target closeup



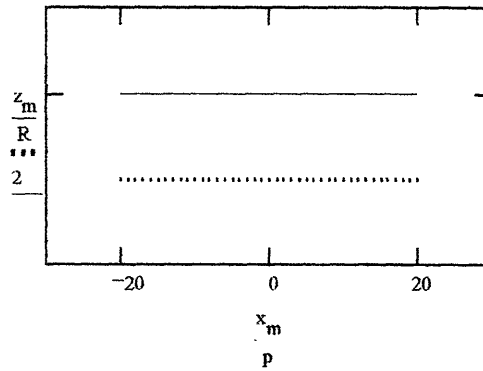
CONSTRUCTION OF IMAGE ON IMAGE SURFACE

Calculate phase delay of downward (-z) travelling planewave incident on target relative to peak $\max(z(x))$, for each of m points of target surface

$$\frac{\max(z)}{R} = 1 \quad \frac{\min(z)}{R} = 1 \quad \Phi_m = -k \cdot (z_m - \max(z))$$

$$\min(\Phi) = 0 \quad \text{always zero! (at peak)}$$

excess phase (rad) due to target features = $\max(\Phi) = 0$



For the image, calculate the phase delay of the upward reflection from surface to image for each point on the surface. This will be the

for flat surfaces

wavenumber k times the distance traversed D , for each scatterer at (x_m, z_m) to each screen point (X_n, Z_n) .

$$\Delta z = R$$

$$D(n, m) := \sqrt{(X_n - x_m)^2 + (Z_n - z_m)^2}$$

$$D = \sqrt{(X_n - x_m)^2 + R^2}$$

Now create image on screen by summing each delayed surface element, together with its phasefront delay from the original planewave source (here =0)

$$E_n = \sum_m e^{-\frac{(x_m)^2}{2(.5-w)^2}} \cdot e^{-j \cdot (k \cdot D(n, m) + \Phi_m)}$$

Huygens Sum,
Gaussian illumination

$$\max E = \max(E)$$

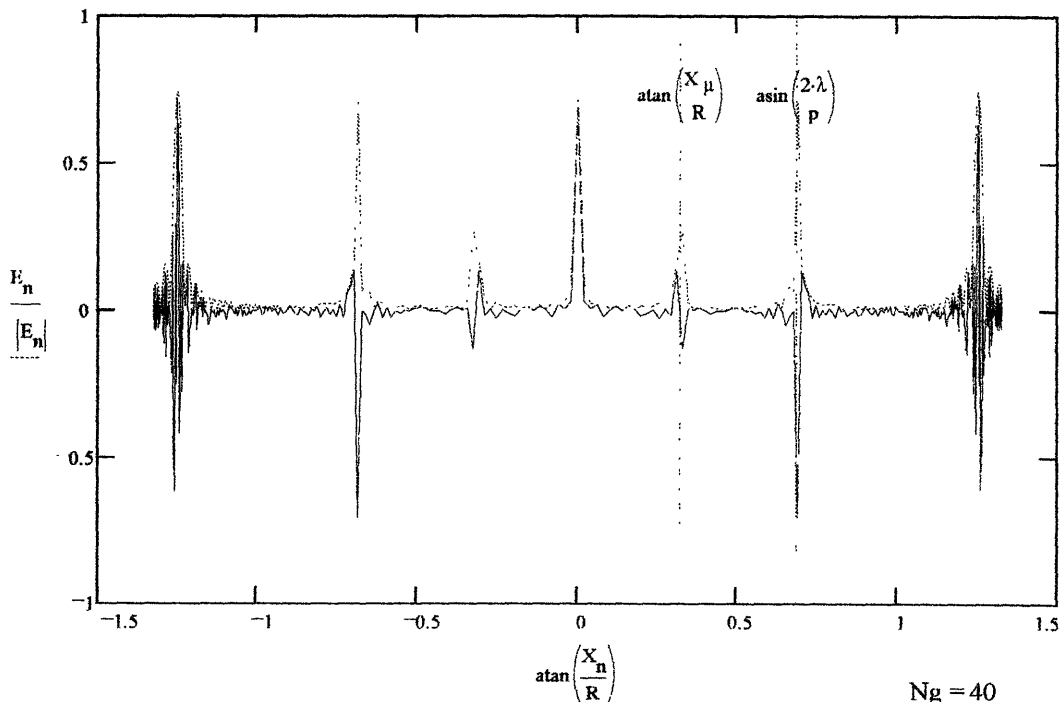
$$E_n := \frac{E_n}{\max E}$$

normalize

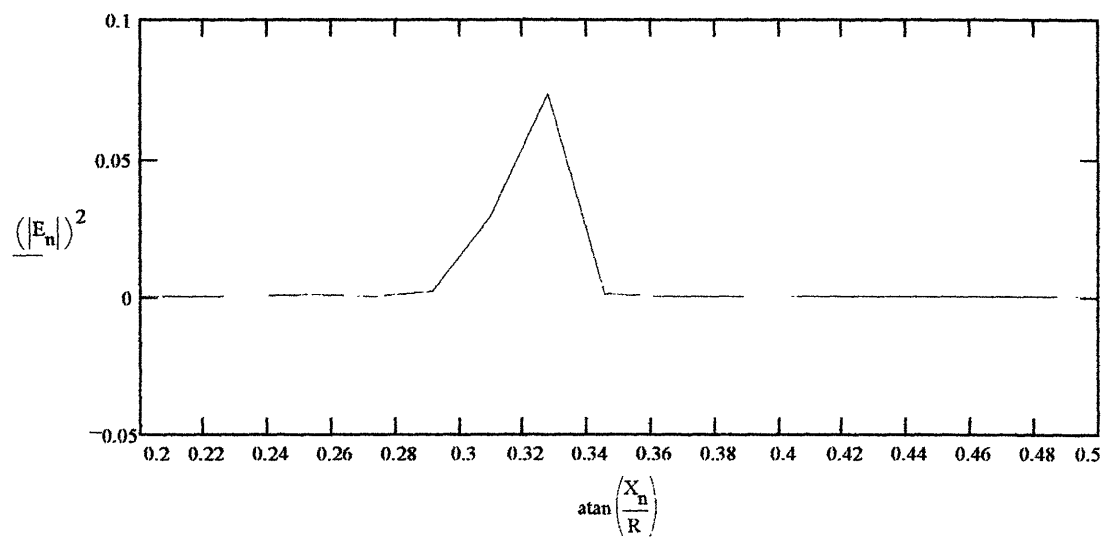
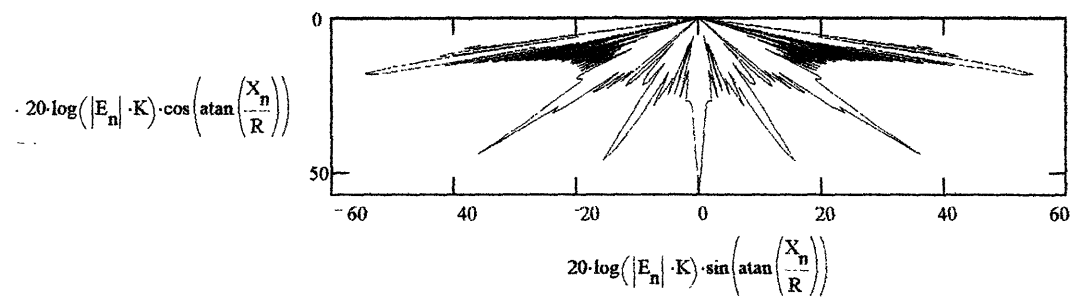
As a check, classical diffraction theory predicts orders at

$$\mu := \text{asin}\left(1 \cdot \frac{\lambda}{p}\right) \quad \mu = 0.322$$

$$X_\mu = R \cdot \frac{\sin(\mu)}{\sqrt{1 - \sin(\mu)^2}}$$



$$K := 10^3$$



+1 ORDER order width= 40 mrad

FOURIER METHOD

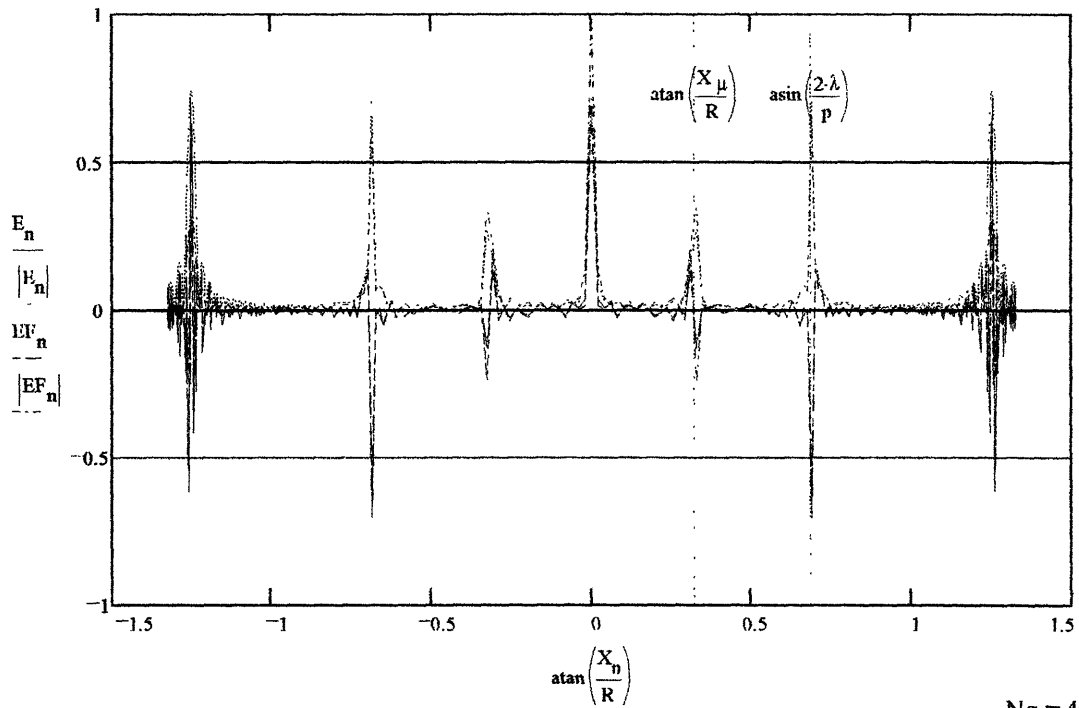
$$a = \frac{p}{4}$$

$$EF_n := \sum_m e^{-j \cdot k \cdot D(n,m)} \cdot \frac{\sin\left(\pi \cdot \frac{X_n - X_m}{D(n,m)} \cdot a\right)}{\left(\pi \cdot \frac{X_n - X_m}{D(n,m)} \cdot \frac{1}{\lambda}\right)}$$

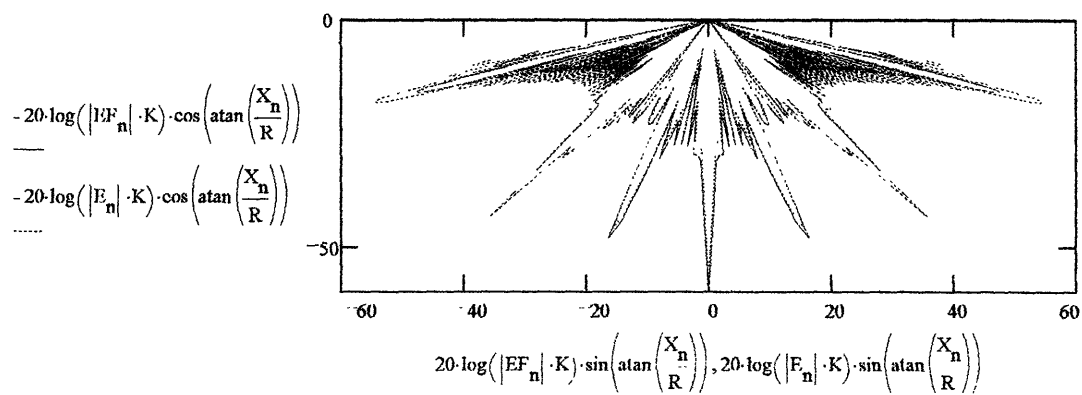
Fourier Sum,
uniform illumination

$$\max EF := \max(EF)$$

$$EF_n = \frac{EF_n}{\max EF}$$



Ng = 40



Fourier Method, addition of curvature to grating

$$\theta := \frac{p}{.1 \cdot R}$$

$$R = 0.01$$

$$m := 0..Ng \quad x_m := \left(m - \frac{Ng}{2}\right) \cdot p \cdot \cos\left[\left(m - \frac{Ng}{2}\right) \cdot \theta\right]$$

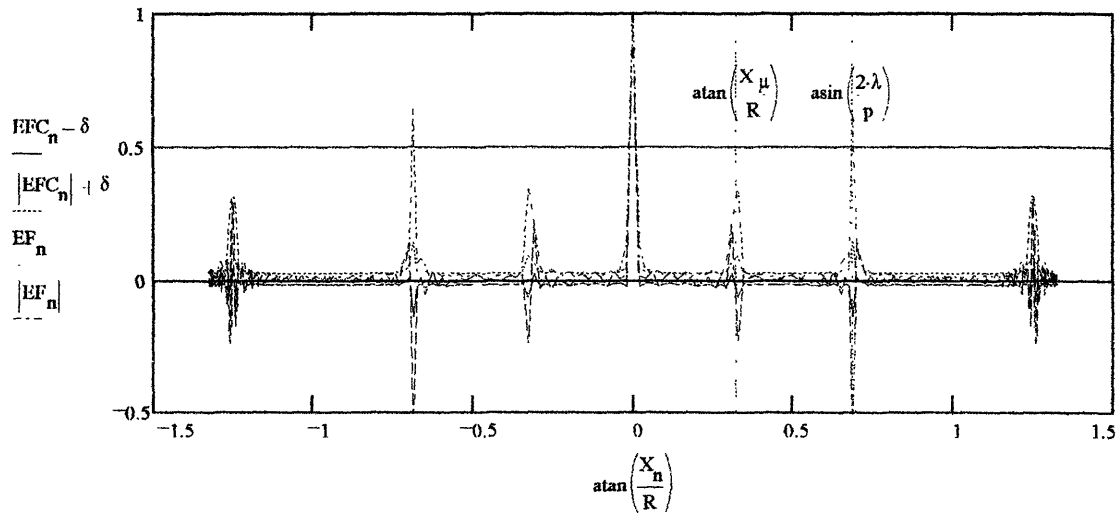
$$z_m := R \cdot \left[1 - \sin\left[\left(m - \frac{Ng}{2}\right) \cdot \theta\right]\right]$$

$$EFC_n := \sum_m e^{-j \cdot k \cdot D(n,m)} \cdot \frac{\sin\left[\pi \frac{X_n - x_m}{D(n,m)} \cdot \frac{a}{\lambda} - \left(m - \frac{Ng}{2}\right) \cdot \theta\right]}{\pi \frac{X_n - x_m}{D(n,m)} \cdot \frac{1}{\lambda} - \left(m - \frac{Ng}{2}\right) \cdot \theta}$$

$$\max EFC = \max(EFC)$$

$$EFC_n := \frac{EFC_n}{\max EFC}$$

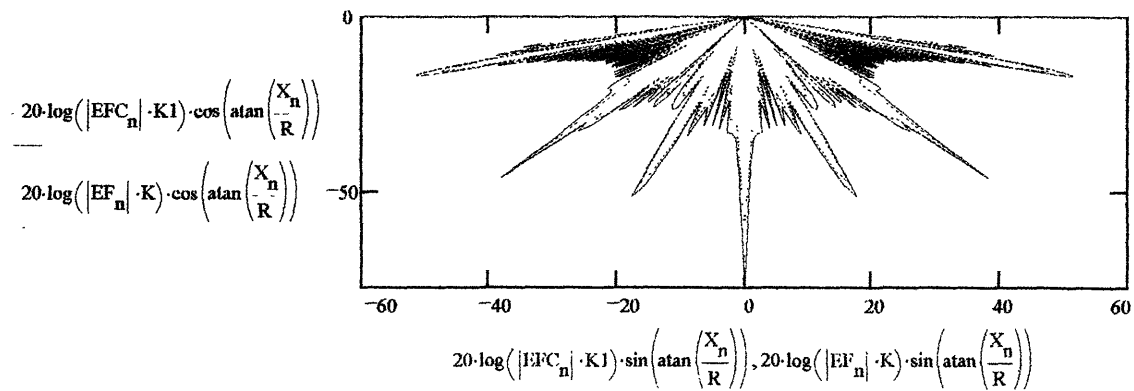
$$\delta := .02$$



$$Ng = 40$$

$$K1 := K \cdot 8$$

(note power loss and broadening with curved grating [solid line])



Fourier Method, with curvature to grating, Effect of duty cycle (a/p)

$$\theta := \frac{p}{.1 \cdot R} \quad R = 0.01$$

$$EFC_n \text{ previously computed with } \frac{a}{p} = 0.25$$

$$a := \frac{p}{2}$$

$$EF_n := \sum_m c^j \cdot k \cdot D(n, m) \cdot \frac{\sin \left| \pi \frac{X_n - x_m}{D(n, m)} \cdot \frac{a}{\lambda} - \left(m - \frac{Ng}{2} \right) \cdot \theta \right|}{\pi \frac{X_n - x_m}{D(n, m)} \cdot \frac{1}{\lambda} - \left(m - \frac{Ng}{2} \right) \cdot \theta}$$

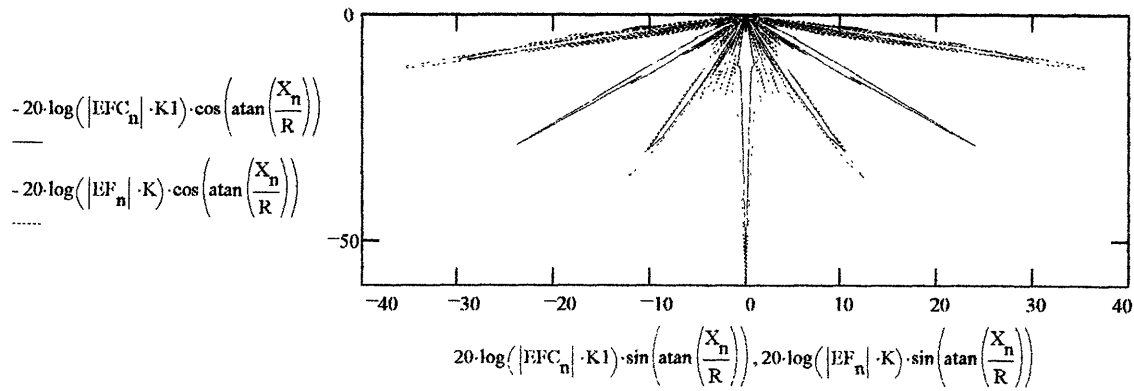
normalize

$$\max EF := \max(EF)$$

$$EF_n := \frac{EF_n}{\max EF}$$

$$K1 := K \cdot (.6)$$

note suppression of second orders, |m|=2



Fourier Method, with curvature to grating, Effect of additive noise (in grating surface height)

$$EFC_n \text{ previously computed with no noise and } a := \frac{p}{4}$$

$$z_m := R \cdot \left[1 - \sin \left(\left(m - \frac{Ng}{2} \right) \cdot \theta \right) \right] + \frac{R}{10} \cdot (\text{rnd}(2) - 1) \quad \text{+/- 10% height variation}$$

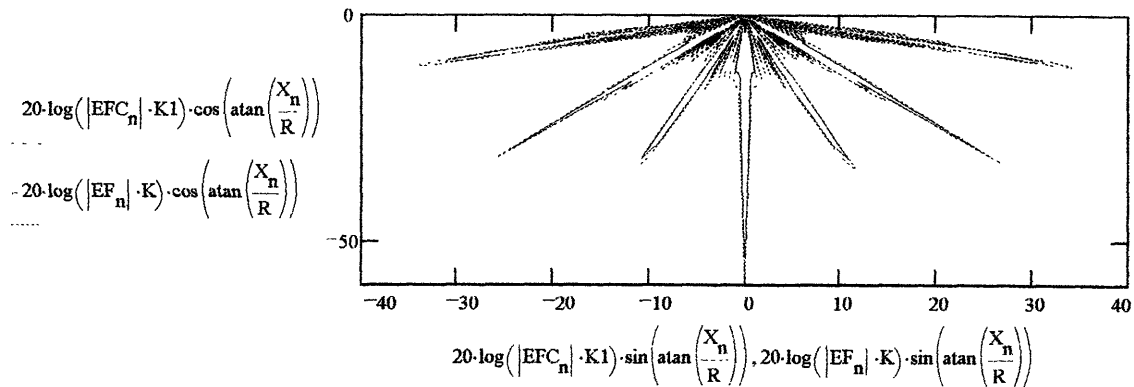
$$EF_n := \sum_m c^j \cdot k \cdot D(n, m) \cdot \frac{\sin \left| \pi \frac{X_n - x_m}{D(n, m)} \cdot \frac{a}{\lambda} - \left(m - \frac{Ng}{2} \right) \cdot \theta \right|}{\pi \frac{X_n - x_m}{D(n, m)} \cdot \frac{1}{\lambda} - \left(m - \frac{Ng}{2} \right) \cdot \theta}$$

normalize

$$\max EF := \max(EF)$$

$$EF_n := \frac{EF_n}{\max EF}$$

$$K1 := K \cdot (.7)$$



note relative immunity to additional height modulations

Repeat analysis for
grating period:

$$p = 10 \cdot 10^{-6} \quad 10 \text{ um}$$

$$N_g = \frac{w}{p} \quad \text{\#gratings illuminated}$$

For quick plots:

$$N_g = 40$$

scale parameter

$$R = 10^{-2} \quad 1 \text{ cm}$$

$$m = 0..N_g$$

$$x_m = -\frac{N_g}{2} \cdot p + p \cdot m$$

flat grating

$$z_m = \text{if}(x_m < 0, R, R)$$

Observer

HORIZONTAL X: N points calculated
(resolution)

$$N = 400$$

$$n = 0..N$$

flat, +/- Xmax
uniform, symmetric

$$X_{\max} = 4 \cdot R$$

$$X_n = -X_{\max} + \frac{n}{N} \cdot 2 \cdot X_{\max}$$

VERTICAL Z: Flat screen, Z(X)=2R

target outline on image screen

$$b = \frac{x_{N_g}}{X_{\frac{N}{2}-1}}$$

$$Z_n = \text{if}(X_n, 2 \cdot R, 2 \cdot R)$$

$$zz_n = \text{if}\left(\left|n - \frac{N}{2}\right| < b, 1, 0\right)$$

Additional phase

$$\Phi_m = k \cdot z_m - \max(z)$$

Distance function

$$D(n, m) = \sqrt{(X_n - x_m)^2 + (Z_n - z_m)^2}$$

Huygens Sum,
Gaussian illumination

$$E_n = \sum_m c \cdot \frac{x_m^2}{2 \cdot (5 \cdot w)^2} \cdot e^{-j \cdot (k \cdot D(n, m) + \Phi_m)}$$

normalize

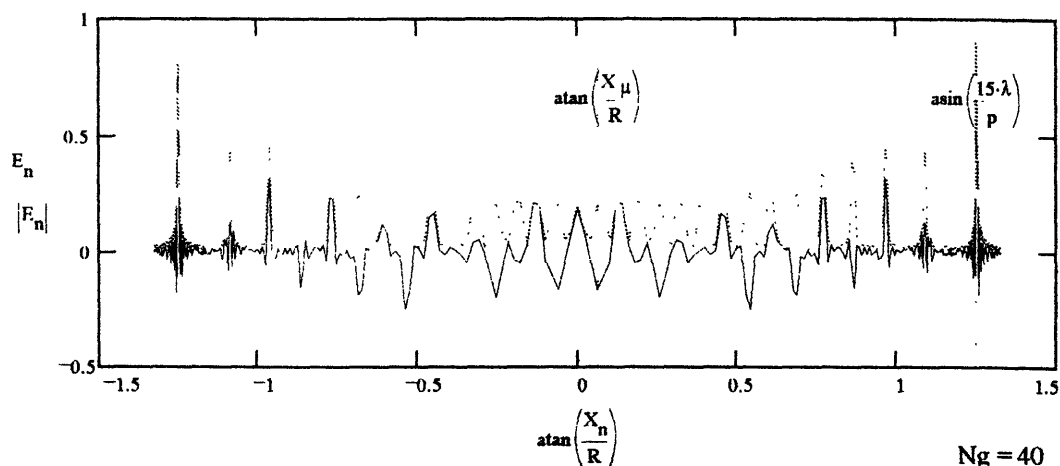
$$\max E = \max(E)$$

$$E_n = \frac{E_n}{\max E}$$

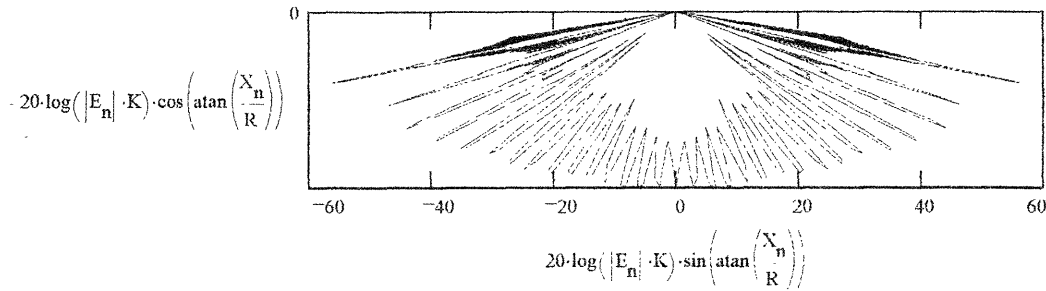
As a check, classical diffraction theory predicts orders at

$$\mu = \text{asin}\left(1 - \frac{\lambda}{p}\right) \quad \mu = 0.063$$

$$X_\mu = R \cdot \frac{\sin(\mu)}{\sqrt{1 - \sin(\mu)^2}}$$



$$K := 10^3$$



FOURIER METHOD

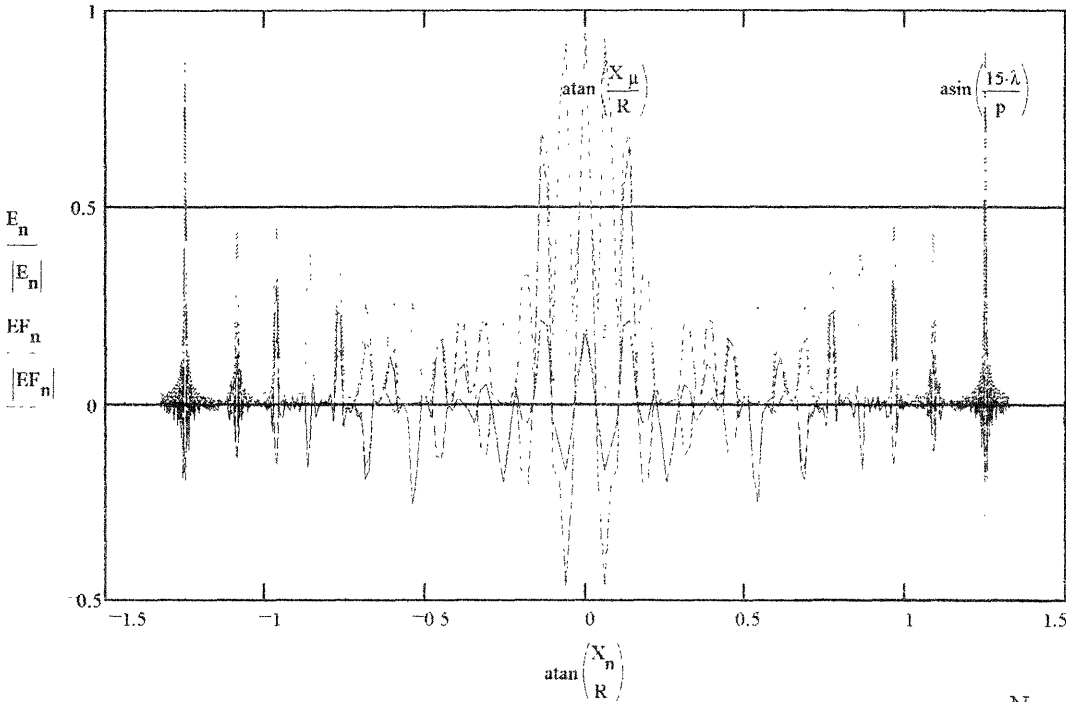
$$a = \frac{p}{4}$$

$$EF_n = \sum_m e^{-j \cdot k \cdot D(n,m)} \cdot \frac{\sin\left(\pi \cdot \frac{X_n - X_m}{D(n,m)} \cdot \frac{a}{\lambda}\right)}{\left(\pi \cdot \frac{X_n - X_m}{D(n,m)} \cdot \frac{1}{\lambda}\right)}$$

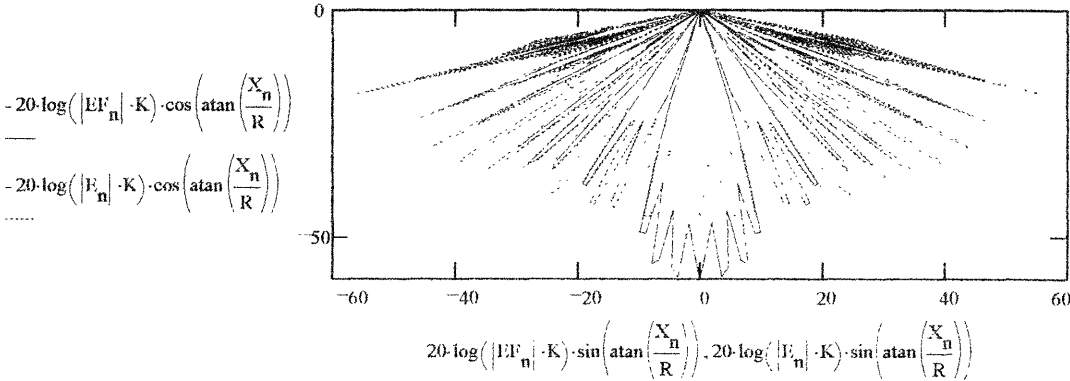
Fourier Sum,
uniform illumination

$$\max EF = \max(EF)$$

$$EF_n = \frac{EF_n}{\max EF}$$



$$Ng = 40$$



Fourier Method, addition of curvature to grating

$$\theta := \frac{p}{1 \cdot R}$$

$$m := 0 \dots Ng$$

$$x_m := \left(m - \frac{Ng}{2}\right) \cdot p \cdot \cos\left[\left(m - \frac{Ng}{2}\right) \cdot \theta\right]$$

$$R = 0.01$$

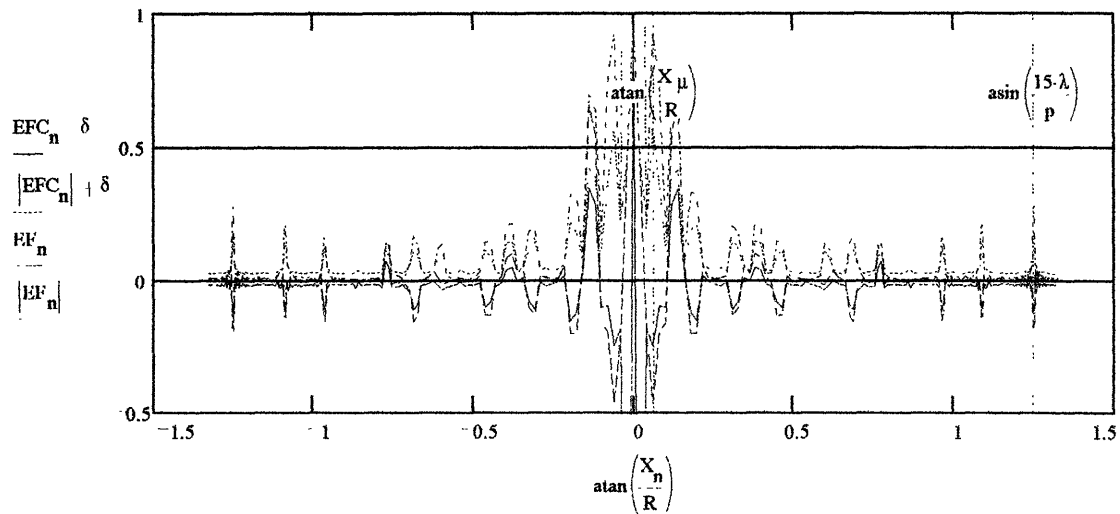
$$z_m := R \cdot \left[1 - \sin\left[\left(m - \frac{Ng}{2}\right) \cdot \theta\right]\right]$$

$$EFC_n := \sum_m e^{-j \cdot k \cdot D(n,m)} \cdot \frac{\sin\left[\pi \frac{X_n - x_m}{D(n,m)} \frac{a}{\lambda} - \left(m - \frac{Ng}{2}\right) \cdot \theta\right]}{\pi \frac{X_n - x_m}{D(n,m)} \frac{1}{\lambda} - \left(m - \frac{Ng}{2}\right) \cdot \theta}$$

$$\max EFC := \max(EFC)$$

$$EFC_n := \frac{EFC_n}{\max EFC}$$

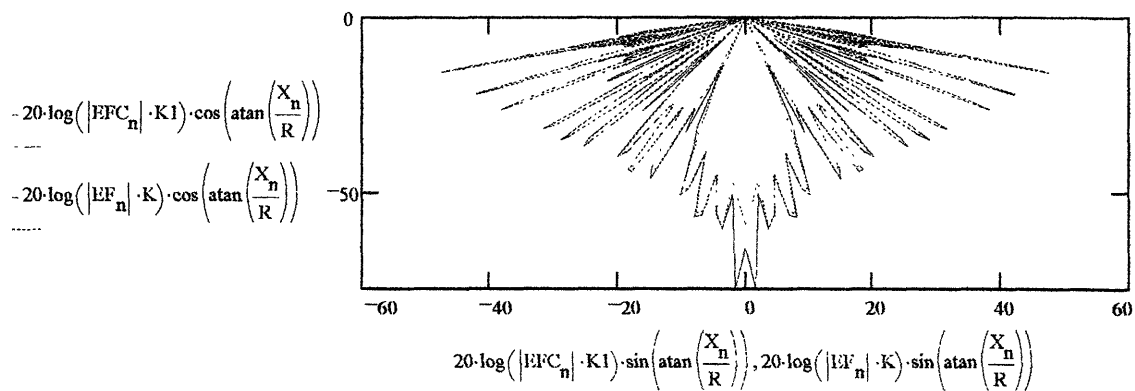
$$\delta := .02$$



$$Ng = 40$$

$$K1 := K \cdot 2$$

(note power loss and broadening with curved grating [solid line])



Fourier Method, with curvature to grating, Effect of duty cycle (a/p)

$$\theta = \frac{p}{1 \cdot R} \quad R = 0.01$$

EFC_n previously computed with $\frac{a}{p} = 0.25$

$$a = \frac{p}{2}$$

$$EF_n = \sum_m e^{j \cdot k \cdot D(n,m)} \frac{\sin \left[\pi \frac{X_n - x_m}{D(n,m)} \frac{a}{\lambda} - \left(m - \frac{Ng}{2} \right) \cdot \theta \right]}{\pi \frac{X_n - x_m}{D(n,m)} \frac{1}{\lambda} - \left(m - \frac{Ng}{2} \right) \cdot \theta}$$

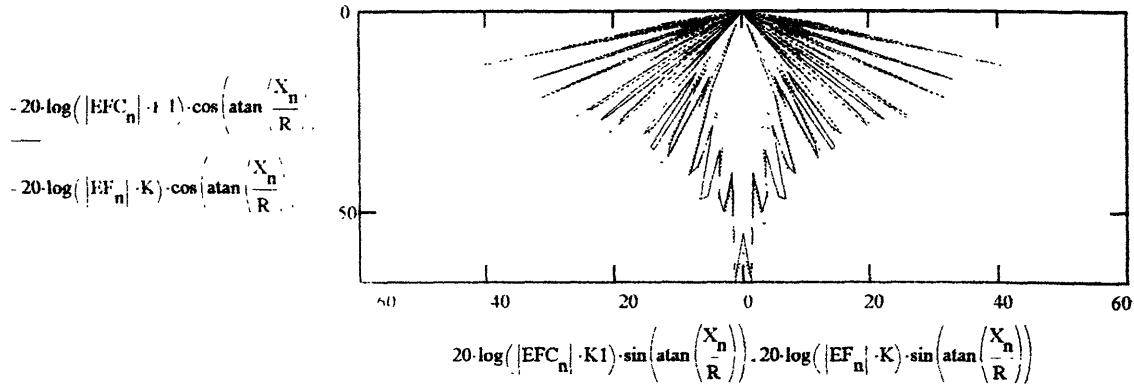
normalize

$$\max EF = \max(EF)$$

$$EF_n = \frac{EF_n}{\max EF}$$

$$K1 = K \cdot (.6)$$

note suppression of even orders, $|m|=2n$



Fourier Method, with curvature to grating, Effect of additive noise (in grating surface height)

EFC_n previously computed with no noise and $a = \frac{p}{4}$

$$z_m = R \left[1 - \sin \left[m - \frac{Ng}{2} \right] \cdot \theta \right] + \frac{R}{10} \cdot (\text{rnd}(2) - 1) \quad \text{+/- 10% height variation}$$

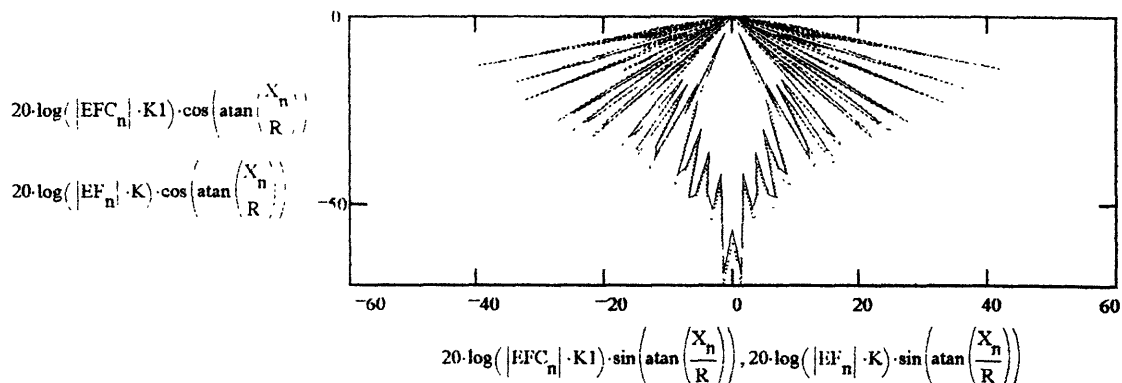
$$EF_n = \sum_m e^{j \cdot k \cdot D(n,m)} \frac{\sin \left[\pi \frac{X_n - x_m}{D(n,m)} \frac{a}{\lambda} - \left(m - \frac{Ng}{2} \right) \cdot \theta \right]}{\pi \frac{X_n - x_m}{D(n,m)} \frac{1}{\lambda} - \left(m - \frac{Ng}{2} \right) \cdot \theta}$$

normalize

$$\max EF = \max(EF)$$

$$EF_n = \frac{EF_n}{\max EF}$$

$$K1 = K \cdot (.7)$$



Repeat analysis for
grating period:

$$p = 74 \cdot 10^{-6} \text{ m} \quad .74 \text{ um}$$

"Rainbow box"

$$N_g = \frac{w}{p} \quad \# \text{ gratings illuminated}$$

$$\lambda = 632.8 \cdot 10^{-9} \text{ m}$$

$$k = \frac{2\pi}{\lambda}$$

$$w = 2 \cdot 10^{-3} \text{ m}$$

$$N_g = 2703 \cdot 10^3$$

Wave analyzer -- agb 11/20/94

- 1.) Huygens sum over point scatterers
- 2.) Sum of Fourier integrals
- 3.) Effect of curvature
- 4.) Effect of duty cycle variation
- 5.) Effect of spatial noise (grating surface irregularity)

For quick plots: $N_g = 40$

scale parameter $R = 10^{-2} \text{ m} = 1 \text{ cm}$

$$m = 0 \dots N_g$$

$$x_m = \frac{N_g}{2} p + p m$$

flat grating

$$z_m = \text{if } x_m < 0, R, R,$$

Observer

HORIZONTAL X: N points calculated (resolution)

$$N = 400$$

$$n = 0 \dots N$$

flat, +/- Xmax
uniform, symmetric

$$X_{\max} = 4 R$$

$$X_n = -X_{\max} + \frac{n}{N} 2 X_{\max}$$

VERTICAL Z: Flat screen, $Z(X)=2R$

$$b = \frac{N_g}{\frac{X_N}{2} - 1}$$

$$Z_n = \text{if } X_n, 2 R, 2 R$$

target outline on image screen

$$zz_n = \text{if } \left| n - \frac{N}{2} \right| < b, 1, 0$$

Additional phase

$$\phi_m = k \cdot z_m \cdot \max(\cdot)$$

Distance function

$$D(n, m) = \sqrt{X_n^2 + z_n^2} + \sqrt{X_m^2 + z_m^2}$$

Huygens Sum,

Gaussian illumination

$$E_n = \sum_m e^{-\frac{1}{2} \left(\frac{X_m}{w} \right)^2} e^{-i k D(n, m) + \phi_m}$$

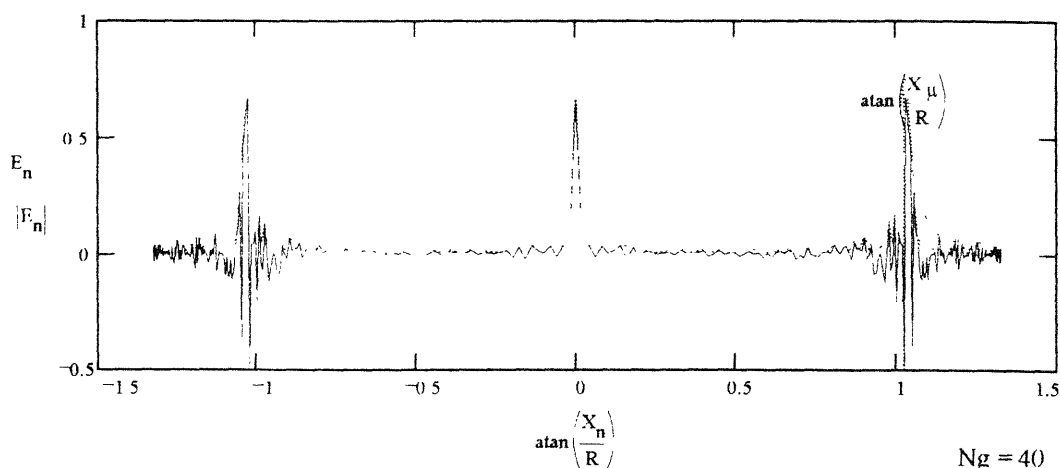
normalize

$$\frac{E_n}{\max(E)} = \frac{E_n}{\max(E)}$$

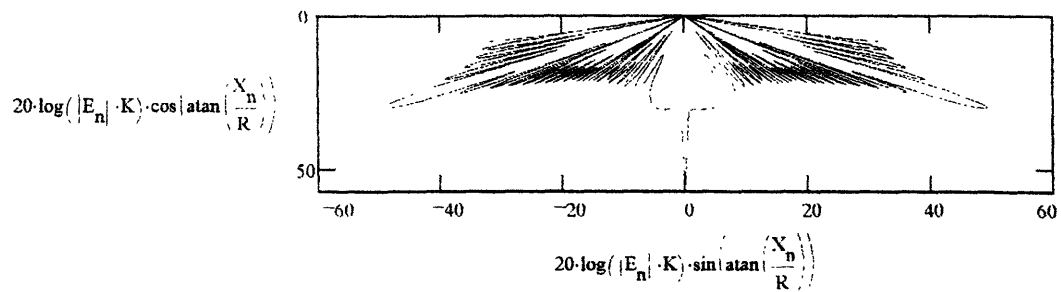
As a check, classical diffraction theory predicts orders at

$$\mu = \sin^{-1} \frac{\lambda}{p} \quad \mu = 1.026$$

$$X_\mu = R \cdot \frac{\sin(\mu)}{\sqrt{1 - \sin^2(\mu)}}$$



$$K = 10^3$$



FOURIER METHOD

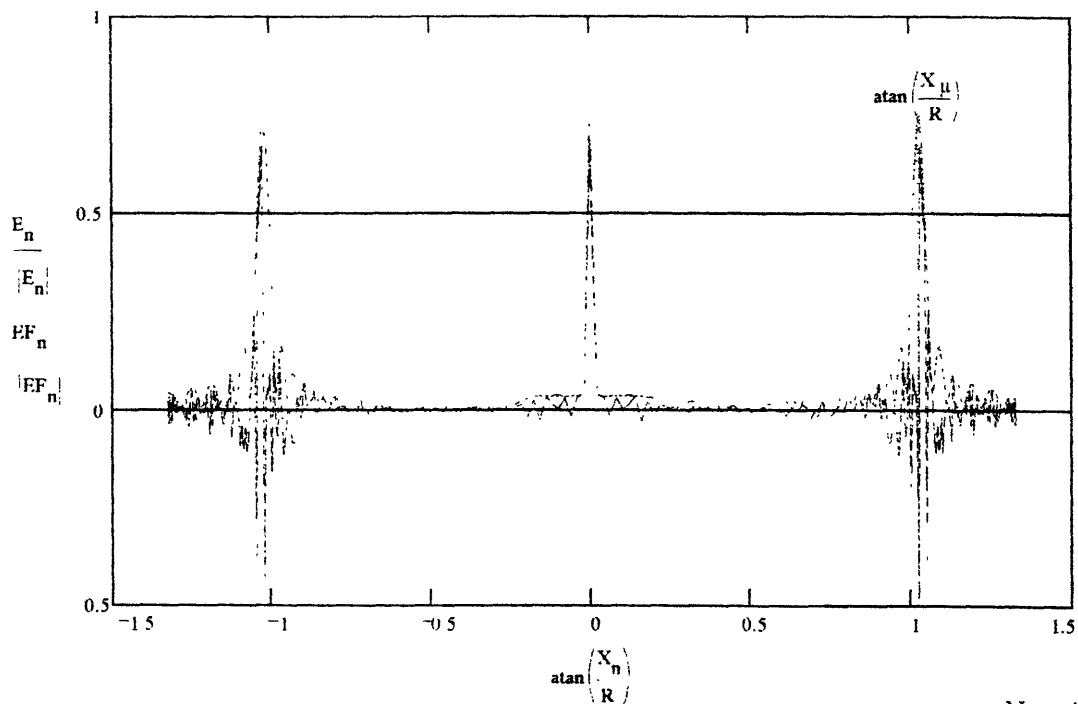
$$a = \frac{p}{4}$$

$$EF_n = \sum_m e^{i k D(n,m)} \frac{\sin \pi \frac{X_n - X_m}{D(n,m)} \frac{a}{\lambda}}{\pi \frac{X_n - X_m}{D(n,m)} \frac{1}{\lambda}}$$

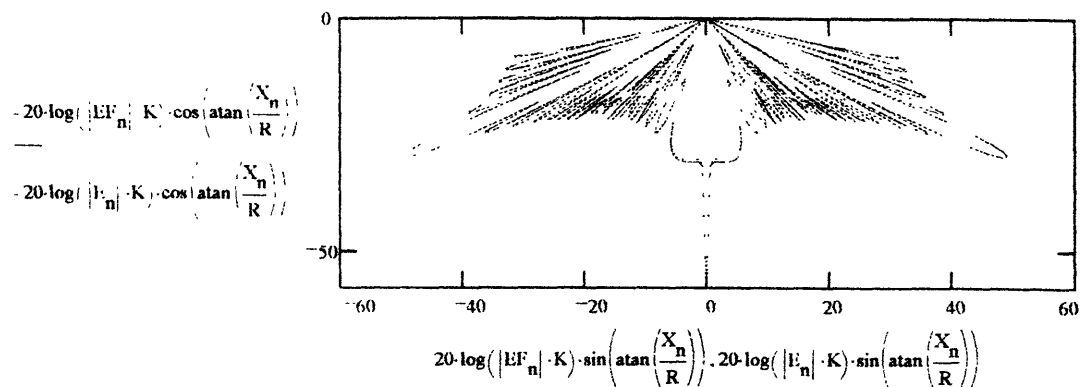
Fourier Sum,
uniform illumination

$$\max EF = \max(EF)$$

$$EF_n = \frac{EF}{\max EF}$$



$$Ng = 40$$



Fourier Method, addition of curvature to grating

$$0 = \frac{p}{1-R}$$

$$R = 0.01$$

$$m = 0..Ng$$

$$x_m = \left(m - \frac{Ng}{2}\right) \cdot p \cdot \cos\left[\left(m - \frac{Ng}{2}\right) \cdot 0\right]$$

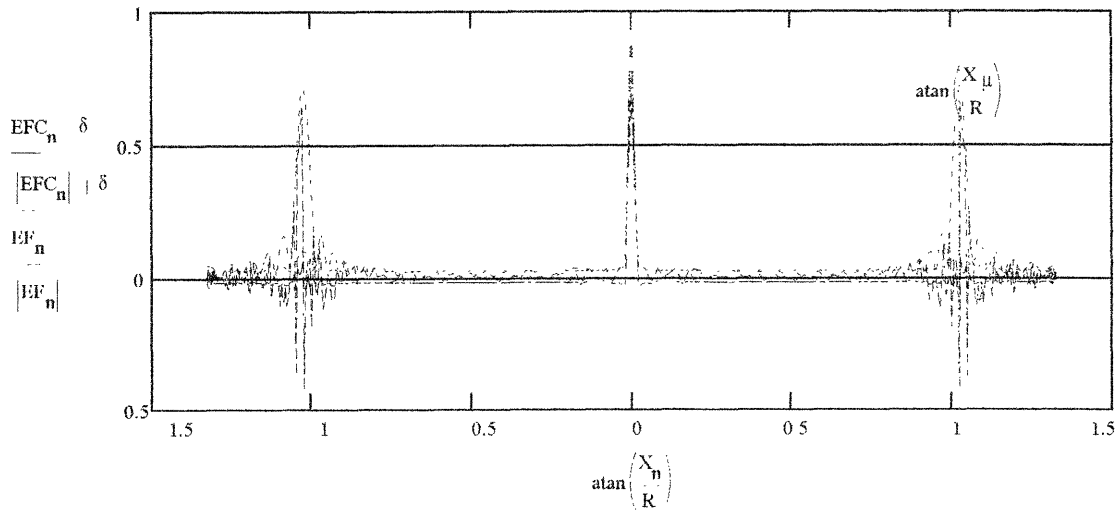
$$z_m = R \left[1 - \sin\left[\left(m - \frac{Ng}{2}\right) \cdot 0\right]\right]$$

$$EFC_n = \sum_m e^{j \cdot k \cdot D(n,m)} \cdot \frac{\sin\left[\pi \frac{X_n - x_m}{D(n,m)} \cdot \frac{a}{\lambda} - \left(m - \frac{Ng}{2}\right) \cdot 0\right]}{\pi \frac{X_n - x_m}{D(n,m)} \cdot \frac{1}{\lambda} - \left(m - \frac{Ng}{2}\right) \cdot 0}$$

$$\max EFC = \max(EFC)$$

$$EFC_n = \frac{EFC_n}{\max EFC}$$

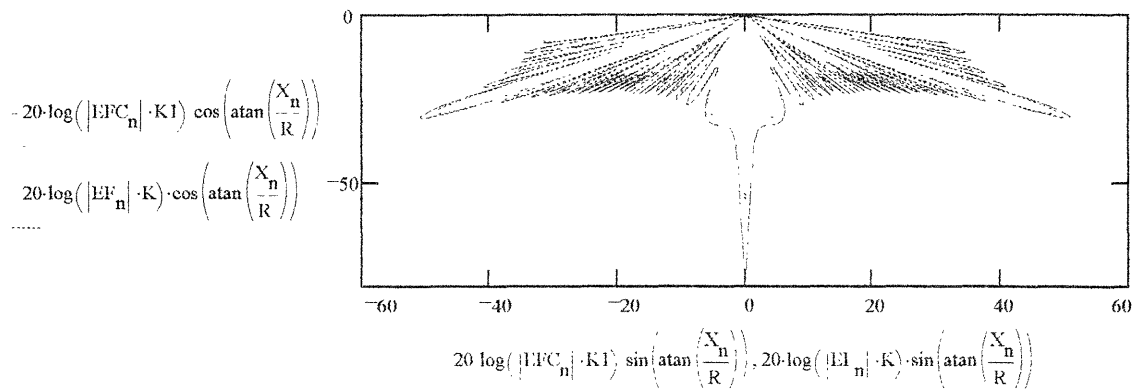
$$\delta = .02$$



$$Ng = 40$$

$$K1 = K \cdot 12$$

(note power loss and broadening with curved grating [solid line])



Fourier Method, with curvature to grating, Effect of duty cycle (a/p)

$$0 = \frac{P}{1 \cdot R} \quad R = 0.01$$

$$EFC_n \text{ previously computed with } \frac{a}{p} = 0.25$$

$$a = \frac{p}{2}$$

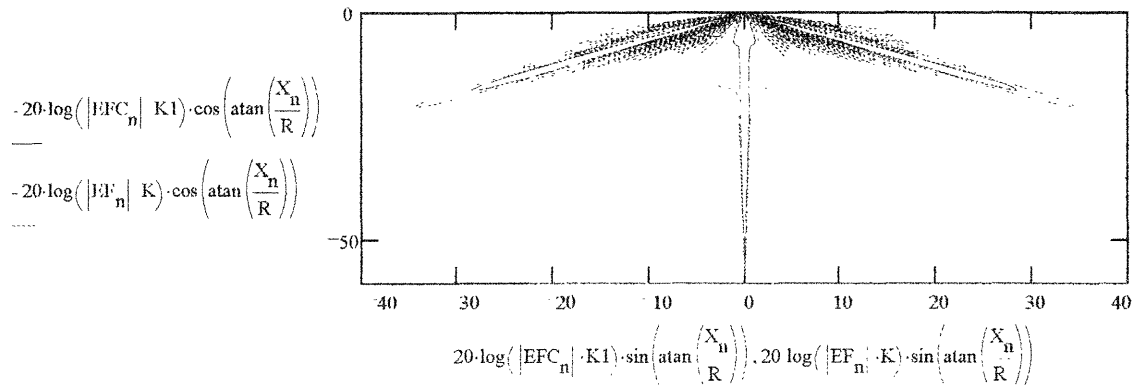
$$EF_n = \sum_m e^{j \cdot k \cdot D(n, m)} \cdot \frac{\sin \left[\pi \cdot \frac{X_n - x_m}{D(n, m)} \cdot \frac{a}{\lambda} - \left(m - \frac{Ng}{2} \right) \cdot \theta \right]}{\pi \cdot \frac{X_n - x_m}{D(n, m)} \cdot \frac{1}{\lambda} - \left(m - \frac{Ng}{2} \right) \cdot \theta}$$

normalize

$$\max EF = \max(EF)$$

$$EF_n = \frac{EF_n}{\max EF}$$

$$K1 = K \cdot (.6)$$



Fourier Method, with curvature to grating, Effect of additive noise (in grating surface height)

$$EFC_n \text{ previously computed with no noise and } a = \frac{p}{4}$$

$$z_m = R \cdot \left[1 - \sin \left[\left(m - \frac{Ng}{2} \right) \cdot \theta \right] \right] + \frac{R}{10} \cdot (\text{rnd}(2) - 1) \quad \text{+/- 10% height variation}$$

$$EF_n = \sum_m e^{j \cdot k \cdot D(n, m)} \cdot \frac{\sin \left[\pi \cdot \frac{X_n - x_m}{D(n, m)} \cdot \frac{a}{\lambda} - \left(m - \frac{Ng}{2} \right) \cdot \theta \right]}{\pi \cdot \frac{X_n - x_m}{D(n, m)} \cdot \frac{1}{\lambda} - \left(m - \frac{Ng}{2} \right) \cdot \theta}$$

normalize

$$\max EF = \max(EF)$$

$$EF_n = \frac{EF_n}{\max EF}$$

$$K1 = K \cdot (.7)$$

interrupted

